

LYMAN BREAK GALAXIES AT REDSHIFT $Z \sim 3$: SURVEY DESCRIPTION AND FULL DATA SET¹

CHARLES C. STEIDEL²

California Institute of Technology, MS 105–24, Pasadena, CA 91125

KURT L. ADELBERGER³

Harvard-Smithsonian Center for Astrophysics, 60 Garden St., Cambridge, MA 02139

ALICE E. SHAPLEY

California Institute of Technology, MS 105–24, Pasadena, CA 91125

MAX PETTINI

Institute of Astronomy, Madingley Road, Cambridge CB3 0HA, UK

MARK DICKINSON AND MAURO GIAVALISCO

Space Telescope Science Institute, 3700 San Martin Drive, Baltimore, MD 21218

ABSTRACT

We present the basic data for a large ground-based spectroscopic survey for $z \sim 3$ “Lyman break galaxies” (LBGs), photometrically selected using rest-UV colors from very deep images in 17 high Galactic latitude fields. The total survey covers an area of 0.38 square degrees, and includes 2347 photometrically-selected candidate LBGs to an apparent \mathcal{R}_{AB} magnitude limit of 25.5. Approximately half of these objects have been observed spectroscopically using the Keck telescopes, yielding 940 redshifts with $\langle z \rangle = 2.96 \pm 0.29$. We discuss the images, photometry, target selection, and the spectroscopic program in some detail, and present catalogs of the photometric and spectroscopic data, made available in electronic form. We discuss the general utility of conducting nearly-volume-limited redshift surveys in prescribed redshift intervals using judicious application of photometric pre-selection.

Subject headings: galaxies: evolution

1. INTRODUCTION

The advent of 10-m class telescopes in the mid-1990s provided for the first time the capability of relatively routine spectroscopic observations of galaxies at very high redshifts (e.g., Steidel et al. 1996a).

¹Based, in part, on data obtained at the W.M. Keck Observatory, which is operated as a scientific partnership among the California Institute of Technology, the University of California, and NASA, and was made possible by the generous financial support of the W.M. Keck Foundation.

²Packard Fellow

³Harvard Society Junior Fellow

However, as was well-known from the most ambitious apparent-magnitude selected surveys conducted on 4m-class telescopes (e.g., Lilly et al. 1996; Ellis et al. 1996) and early work on the Keck telescopes (e.g., Songaila et al. 1994, Cohen et al. 1996, Cowie et al. 1996), simply observing fainter galaxies is a relatively inefficient means of assembling significant statistical samples at high redshift, and even at the limit of 10-m class telescopes for complete spectroscopic samples ($R \sim 24$) the sampling beyond $z \sim 1$ is relatively sparse. Meanwhile, the technique of “photometric redshifts” had gained considerable new impetus as imaging surveys such as the Hubble Deep Field campaigns (Williams et al. 1996) reach far deeper than current spectroscopic capabilities, and some insights into the galaxy formation process are possible with redshift estimates only.

Our approach has been based on the assertion that the information gained from spectroscopy is essential for addressing many scientific issues. The technique for acquiring the spectroscopic information might be thought of as a hybrid that lies somewhere between photometric redshifts and traditional flux-limited “blind” redshift surveys. “Photometric pre-selection”, where objects are chosen for spectroscopy based on coarse features in their spectral energy distributions that can be recognized from simple broad or intermediate-band photometry, introduces both advantages and complications (see, e.g., Steidel 2000, Adelberger 2002). The technique has several practical advantages: for example, one can focus on a particular range of redshift using appropriately chosen color criteria, so that the imposition of an apparent magnitude limit is nearly equivalent to imposing a luminosity limit. If the selection function is relatively narrow in redshift, one can construct nearly volume-limited samples, so that one can include a significant range in absolute magnitude at a given redshift without observing many objects outside of the targeted redshift range. Photometric pre-selection mitigates many issues inherent in flux limited surveys, such as very broad redshift selection functions where different kinds of objects are selected at the “front” and the “back” of the survey volume. There is also a distinctly practical advantage of efficiency for spectroscopy on large telescopes— at an apparent magnitude of $R \sim 25$, the surface density of faint galaxies has reached ~ 30 per square arc minute, much too dense for complete spectroscopy without observing the same patch of sky many times using different slit masks. The redshift distribution of such a sample would be extremely broad ($z \sim 0.1 - 5$), and typical spectroscopic observations optimized over less than an octave in wavelength would fail to measure redshifts for a large fraction⁴ of the targeted galaxies. The gain in efficiency for studying galaxies in a particular constrained cosmological volume can be as large as a factor of 10–25, depending on the chosen redshift range and nature of the selection on coarse spectral properties. With photometric pre-selection, one knows *a priori* the approximate redshift of the targets and thus the optimal spectroscopic configuration (wavelength range, grating and blaze wavelength, spectral resolution required) that balances efficiency and information content. Disadvantages of photometric pre-selection include increased complexity of the selection function, the need for higher quality initial images for target selection, and more difficult post-facto analysis to understand issues of completeness. Many of these issues are discussed in some detail in Steidel et al. (1999) and Adelberger (2002).

The use of the Lyman limit of hydrogen at 912 Å in the rest frame of the galaxies is only one example of all potential uses of photometric pre-selection; more recently, Adelberger (2000) and Davis et al. (2002) have applied photometric culling for selecting samples with $z = 1.0 \pm 0.1$ and $z \gtrsim 0.7$, respectively. The many on-going searches for “Extremely Red Objects” selected by virtue of relatively extreme optical-IR colors are similar in spirit (e.g., McCarthy et al. 2001; Daddi et al. 2002), as are searches targeting high-redshift objects selected by their IR colors (e.g., Labbé et al. 2003). Targeting $z \sim 3$ for our initial survey grew out of purely practical issues: it is the lowest redshift where the Lyman limit can be recognized from the ground using

⁴For example, one would want to be optimized in the 7000 – 10000 Å range for $z \sim 0.9 - 1.5$, in the 4000-6000 Å range for $z \gtrsim 2.5$, and in either the near-UV or the near-IR for redshifts in between.

broad-band photometry (Guhathakurta, Tyson, & Majewski 1990; Steidel & Hamilton 1992, 1993) because the standard U band (or, U_n , in our case) is centered near 3550 Å.

The use of broad-band colors to select objects for subsequent spectroscopy has long been a standard technique to search for quasars (e.g., Green 1976; Koo & Kron 1988; Warren, Hewett, & Osmer 1991), and the suggestion of using colors to identify primeval galaxies was made as early as 25 years ago (Meier 1976), with searches commencing soon after (e.g., Koo & Kron 1980). However, most of the early searches for high redshift galaxies depended on an assumed extremely luminous phase expected if massive galaxies formed a large fraction of their stars on a dynamical timescale (motivated by arguments given in, e.g., Eggen, Lynden-Bell, & Sandage 1962 and Partridge & Peebles 1967) and in any case were limited by the relatively poor sensitivity of photographic plates. More stringent constraints on the *existence* of star-forming galaxies at redshifts significantly beyond $z \sim 1$ had to await the first extremely deep CCD imaging surveys. Meanwhile, we were strongly influenced by the results of QSO absorption line studies (e.g. Wolfe et al. 1986; Sargent et al. 1988, 1989; Steidel 1990a,b, Bergeron & Boissé 1991), some of which suggested that relatively normal galaxies may be present at redshifts as high as $z = 2 - 3$.

The general lack of success of most “proto-galaxy” surveys (see, e.g., the review by Pritchet 1994) that focused on the detection of the Lyman α emission line suggested that other techniques using features less susceptible to dust and scattering effects were necessary before high redshift galaxies were written off as non-existent, hopelessly faint, or completely hidden. Most of the emphasis in the galaxy evolution community through the late 1980s and early 1990s was on the so-called “faint blue galaxies” which became especially evident in very deep CCD images of the sky (e.g., Tyson 1988; Cowie et al. 1988; Lilly et al. 1991). The fact that the galaxies were very blue from B to K (Cowie et al. 1988) implied that these objects must lie at redshifts $z \leq 3.5$. Guhathakurta, Tyson, & Majewski (1990) set more explicit limits on the fraction of “faint blue galaxies” to apparent magnitude limits of $R \sim 26$ that could lie at redshifts $z \gtrsim 3$, based on the observed flatness of the spectral energy distributions through the observed U band. They concluded that the fraction of galaxies with $z \gtrsim 3$ was less 7%, and they suspected that it “is likely to be less than 1%-2%”⁵. Steidel & Hamilton (1992, 1993) and Steidel, Pettini, & Hamilton (1995) addressed a somewhat different follow-up question: given knowledge of where to look for a galaxy with a redshift $z \geq 3$, can one either detect it or set limits on its luminosity using a technique tuned to find even intrinsically faint objects at the known redshift of Lyman limit systems or damped Lyman α systems, even if they have no Lyman α emission? Some success in identifying *candidate* high redshift galaxies resulted from these searches targeting “known” galaxies near the lines of sight to background QSOs. The first spectroscopy of these candidates was however not attempted until the fall of 1995 (Steidel et al. 1996), using the Keck 10m telescope and the Low Resolution Imaging Spectrometer (LRIS; Oke et al. 1995). Unexpected success in measuring spectroscopic redshifts with reasonable integration times suggested that more comprehensive surveys for high redshift galaxies were feasible. This paper represents a superset of the observations made after converging on a uniform approach to candidate selection and spectroscopy.

A number of other practical advantages of working near $z \sim 3$ became clear from the initial spectra: Lyman α emission is not required to confirm redshifts, because a large number of strong interstellar lines in the rest wavelength range 1200-1700 Å falls conveniently in the 4500-6500 Å observed range, where optical spectrographs are efficient and the sky background is relatively dark. Thus, quite unexpectedly, spectroscopic

⁵In fact, with hindsight, the fraction of galaxies to $R = 26$ that satisfy our LBG selection criteria is 6.3%, from our survey in the Q1422+2309 field. This apparently small number says more about the high density of “foreground” objects than about the absence of high redshift objects, and emphasizes why photometric pre-selection is essential for targeting a particular range of redshifts.

identification with a very high success rate was possible to apparent magnitudes $\mathcal{R} \sim 25.5 - 26$, as much as two magnitudes fainter than the reasonable limit for a simple apparent magnitude selected survey that would yield a similar spectroscopic success rate. Of course, there are certainly objects in the targeted redshift range that would not satisfy our color selection criteria and so could not be accounted for even with careful correction for incompleteness (e.g., objects that are reddened with more than $E(B - V) \sim 0.4$, corresponding to $\sim 4 - 5$ magnitudes of internal extinction in the far-UV – Adelberger & Steidel 2000). Other techniques, such as sub-mm or X-ray selection, are required to find such objects. However, by number, objects that satisfy the simple LBG color selection rules are by far the dominant “population” at $z \sim 3$ (Dickinson 2000). Whether they dominate the total star formation rate or energy production rate is still a matter of significant debate (cf. Adelberger & Steidel 2000; Barger, Cowie, & Sanders 1999). It is certainly safest to treat LBGs as a type of object that is common, easy to find using readily available observational facilities, and for which large statistical samples are possible. No doubt our understanding of how LBGs are related to other objects in the $z \sim 3$ universe will improve substantially in the coming years.

The data collected in this paper have been used in a number of more focused investigations on the nature of Lyman break galaxies, their large-scale distribution, their relationship to the diffuse intergalactic medium, and their connection with other high redshift samples of galaxies selected at other wavelengths. For example, subsets of the spectroscopic sample have been used to quantify the clustering strength of $z \sim 3$ LBGs (Steidel et al. 1998; Adelberger et al. 1998; Adelberger et al. 2003) while the photometric samples, together with knowledge of the redshift selection function, have been used to measure clustering from various angular statistics (Giavalisco et al. 1998; Giavalisco & Dickinson 2001; Porciani & Giavalisco 2002). The redshift distribution of a substantial subset of the sample presented here was used, together with the photometric sample, to evaluate the rest-frame far-UV luminosity function (Dickinson 1998; Steidel et al. 1999; Adelberger & Steidel 2000), the range of intrinsic properties represented in the LBG sample, and the likely contribution of UV-selected objects to star formation history and far-IR/sub-mm background. Studies of the near-IR spectra (Pettini et al. 1998, 2001) and near-IR photometry (Shapley et al. 2001) have made use of subsets of the spectroscopic sample presented here, to explore kinematics, chemical abundances, and star-formation histories. The trends discernible in the optical discovery spectra of the LBGs have been explored and quantified by Shapley et al. (2003). The AGN content of the spectroscopic sample has been discussed in a preliminary way by Steidel et al. (2002). Some of the LBGs presented here have been examined at X-ray (Nandra et al. 2002) and sub-mm (Chapman et al. 2000; Chapman et al. 2001) wavelengths. Almost half of the current sample of $z \sim 3$ LBGs was obtained as part of a major effort to quantify the relationship between H I and metals in the intergalactic medium and the star forming galaxies (Adelberger et al. 2003), and has not been used in many of the aforementioned studies because it was not completed until 2002.

It is not our intention to duplicate any of the work that has already been published on the $z \sim 3$ LBG sample, but rather to present the photometry and spectroscopy for the entire sample in as compact a manner as possible. We describe in more detail the overall survey strategy, from a practical point of view, and present some statistics that may prove useful to other workers who might like to make use of some or all of the data. The organization of the paper is as follows: §2 describes the survey imaging data and reductions; §3 summarizes the photometry; §4 describes the photometric selection of candidate LBGs; §5 discusses the spectroscopic observations and analysis of the candidates; §6 summarizes the results for “interloper” objects in the spectroscopic sample, and §7 includes discussions of individual fields in the survey. A short summary of the results is given in §8.

2. IMAGING OBSERVATIONS AND DATA

The imaging data for the 17 fields presented here were obtained during the interval 1994–2000 on a number of telescopes, detailed in Table 1. The imaging filters used were the U_nGR system (supplemented with I band data in most cases, although the I band data were not explicitly used for the $z \sim 3$ LBG project) described in Steidel & Hamilton (1993); it turns out that the U_n filter is essentially identical to the Sloan Digital Sky Survey (SDSS) u' filter (both U_n and SDSS u' cut at 4000 Å on the red side, about 200 Å blue-ward of the standard Johnson U passband). The G filter has the same effective wavelength as the SDSS g' filter, but is slightly narrower. The R filter used for the vast majority of the imaging presented in this paper has a bandpass centered at 6830 Å and a half-power bandwidth of ~ 1250 Å. The filter system passbands are shown in Figure 1.

In general, individual integrations of 900s (R), 1200s (G) and 1800s (U_n) were obtained, with 10–15" dithers between exposures. Wherever possible, the U_n data were obtained within ~ 2 hours of the meridian to minimize atmospheric attenuation and dispersion effects. For all but some of the WHT data, the detectors used were thinned, back-side illuminated Tektronix (SITE) 2048 x 2048 CCDs, with a pixel scale depending on the telescope (see Table 1). The data for Q1422+2309 and Q0302-003 were obtained at the William Herschel Telescope using, respectively, a single 2K x 4K EEV (now Marconi) CCD and a mosaic of 2 such EEV devices. These CCDs have approximately twice the UV quantum efficiency of the SITE devices but suffer from much higher amplitude fringing in the red. With very few exceptions, data obtained under seeing condition worse than 1.3" (FWHM) were excluded, so that the final stacked images average $\sim 1''$ (Table 1). Total integration times varied depending on observing conditions and telescope/camera combinations; these are also summarized in table 1.

The data were flat-fielded using dome flats for G , R , and I band observations, and using a combination of twilight sky and dark sky “superflats” (where flat fields were created by median-combining dis-registered science images after masking out the positions of objects) for the U_n band data. Fringe removal for the I band images (and R for the WHT EEV data) was accomplished using standard techniques. Cosmic rays were identified morphologically on each exposure and masked so as to be excluded in the production of the stacked image. Stacks were produced by combining sub-pixel-registered, photometrically-scaled images in each band and averaging unmasked pixels. Final stacks in each band were then geometrically transformed onto the pixel scale of the R image so that the final images in each band are registered to better than 0.05". To avoid photometric non-uniformities in the survey fields, for all single-CCD data we retained only those image regions receiving the full exposure time in every band.

Several spectrophotometric standard stars from Massey et al. (1988) or from Oke (1990) were observed during each observing night, through each filter, at a range of airmasses. Artificial magnitudes on the AB system for U_n , G , R , and I for each standard were produced by multiplying the effective filter passband (including CCD quantum efficiency and atmospheric attenuation) and the stellar energy distribution. Photometric zero points (reduced to an airmass of 1.0) measured in this way had internal scatter of ± 0.02 magnitudes for G , R , and I filters, and ± 0.03 magnitudes for U_n among different standard star measurements obtained during the same observing run. As discussed in §3 below, the photometric uncertainty achieved in the survey is generally limited by the systematics of object detection, aperture corrections, blending, and sky evaluation and not by the precision of the calibrations. We assumed atmospheric attenuation of 0.56, 0.19, 0.08, and 0.06 magnitudes per airmass for U_n , G , R , and I , respectively; these values were used to reduce the standards observed at a variety of airmasses, and no significant departures from these values were indicated (the internal scatter of the photometry is as good as it can be given the precision of the spectrophotometry).

of the standards we have used). Effective zero points were calculated for each image by using the single (photometric) exposure observed at smallest airmass in each band, and forcing the magnitudes in the stacked image to yield the same magnitudes as in the calibration image. This procedure mitigated uncertainties in the atmospheric attenuation constants and allowed for the inclusion of non-photometric data in the stacks. The photometric zero points were then corrected for Galactic extinction using the relations

$$A(U_n) = 4.8E(B - V); \quad A(G) = 3.7E(B - V); \quad A(\mathcal{R}) = 2.3E(B - V); \quad A(I) = 1.7E(B - V)$$

where $E(B - V)$ was estimated from the relation $E(B - V) = 0.018S_{100}$ and S_{100} is the IRAS 100 μm intensity in MJy sr^{-1} . This extinction calibration is very similar to that advocated by Schlegel, Finkbeiner, & Davis (1998). The adopted Galactic extinction for each field is summarized in Table 2.

The reduced images were astrometrically calibrated, in the case of data obtained at Palomar, using the established plate solution for COSMIC and zero-pointed using several reference stars on the Hubble Space Telescope guide star catalog system. All other data were astrometrically calibrated with reference to the USNO-A2 astrometric catalog (Monet et al. 1996), matching typically 50-100 objects and using a polynomial solution to map the focal plane to the astrometric reference. The typical residuals with respect to the USNO-A2 positions were 0.3-0.4", but we estimate that the internal accuracy for the relative astrometry in all cases is better than $\sim 0.1''$ based on experience in the fine-alignment of slit masks.

3. GALAXY PHOTOMETRY

We adopted a uniform method for performing the galaxy photometry which was maintained throughout the survey; it is nearly identical to that described previously in Steidel & Hamilton (1993), Steidel, Pettini, & Hamilton (1995), and Steidel et al. (1999).

For all survey fields, the image quality was matched in each band by smoothing the data with a Gaussian kernel so that the FWHM of stars was the same to within $\sim 5\%$. In practice, this usually meant that all of the images were smoothed to match the image quality in the U_n band data. We used a modified version of the FOCAS (Valdes 1982) photometry program for the detection and photometry of the galaxies. Briefly, the program was modified to allow for improved measurement of the local sky values and to allow for masking of regions of the image in the detection process.

The detection of objects was performed on the \mathcal{R} band image, after lightly smoothing with the default 2-pixel FWHM smoothing kernel. Objects were “detected” if the number of connected pixels with flux exceeding 3 times the sky σ (of the unsmoothed data) was such that their isophotal area exceeded the size of the seeing disk (typically about 1 square "). In practice, even at the faint limit of our final catalogs ($\mathcal{R} = 25.5$ for all but Q1422+2309) the typical isophotal size of a detected object is ~ 3 square arcseconds, so that the isophotal aperture is roughly equivalent to a 2" diameter circular aperture. The FOCAS “total” magnitude is formed by growing the isophotal detection aperture by a factor of two in area, i.e. equivalent to a $\sim 3''$ diameter aperture at the faint limit of our catalogs. The average aperture corrections (i.e., $m_{\text{iso}} - m_{\text{tot}}$) are nearly independent of apparent magnitude over the range used in the survey, and range from 0.10-0.15 magnitudes for a typical LBG survey field. Simulations described below show that using apertures of this size leads to negligible light loss. The local sky background is evaluated in an “annulus” of specified width (in pixels) outside of this total magnitude aperture, excluding any pixels that are within the detection aperture of any other detected object. An attempt is made to de-blend objects whose detection isophotes are merged by raising the isophotal level until separate objects, each of which satisfied the minimum isophotal size criterion,

are found. The light within the parent total aperture is then divided among the child objects according to the ratio of the luminosity within the raised isophotal apertures. The set of isophotal detection apertures is then transferred to the images in the other passbands, so that colors are measured through identical apertures. When we quote a \mathcal{R} magnitude, we refer to the FOCAS “total” magnitude, while the galaxy colors are measured using the isophotal apertures. Thus, we implicitly assume that there are no significant color gradients in the galaxies, which seems reasonable given that most of the objects faint enough to be LBG candidates are barely resolved in $\sim 1''$ seeing. A final culling of the photometric catalogs is made by requiring that $19.0 \leq \mathcal{R} \leq 25.5$ (except for the Q1422+2309 field, which has a faint limit of $\mathcal{R} = 26.0$; the bright limit ensures that objects which might have been saturated in individual exposures are not included), and that objects are detected in the G band with greater than 3σ significance (otherwise measured $U_n - G$ colors would have no statistical significance). No requirement is made on the U_n magnitude.

For some purposes, we have made use of the image statistics to evaluate the photometric depth of the survey images. We define 1σ limits by $N_{\text{pix}}^{0.5} \sigma_{\text{sky}}$, where N_{pix} is the number of pixels in the detection aperture and σ_{sky} is the RMS pixel to pixel fluctuations in the sky background⁶. Limits defined in this way are used to distinguish between objects that are “detected” in the U_n band and those that are merely limits. In our definition, if the U_n flux in the object aperture exceeds 1σ as described above, the object is considered “detected” and the U_n magnitude assigned is the value appropriate for the measured flux; if the flux in the aperture is less than 1σ the object is assigned a limit that is defined as the magnitude corresponding to the aperture 1σ limit. In Table 2 we show the 1σ limits in each band for each field, for an aperture having an area three times the size of the seeing disk; this aperture approximates the typical isophotal detection aperture for objects at the faint limit of our catalogs. In general, the faintest objects retained in the catalogs ($\mathcal{R} = 25.5$, and $\mathcal{R} = 26.0$ for the Q1422+2309 field) are $\sim 10\sigma$ detections in the \mathcal{R} band. Thus, formally, we expect that the photometric errors for the \mathcal{R} magnitudes are $\lesssim 0.1$ mags (but see below). The expected color uncertainties will of course depend upon the galaxy colors; for objects with the typical colors of LBGs ($G - \mathcal{R} \simeq 0.5$, $U_n - G > 2.0$), the formal uncertainties should be smaller than ~ 0.15 magnitudes in $G - \mathcal{R}$ but (since most U_n magnitudes are close to the 1σ limits) $\sim 0.6 - 0.7$ magnitudes in $U_n - G$ for objects at $\mathcal{R} = 25.5$. At the catalog limit of $\mathcal{R} = 25.5$, objects having the relatively blue $U_n - G$ colors of typical faint galaxies (see Table 2) would have formal color uncertainties in $U_n - G$ of ~ 0.25 mags.

Perhaps more realistic photometric uncertainties have been obtained from extensive simulations in which objects of known colors and magnitudes were added to the data and then recovered and measured using the same photometric procedures as for the real data. The results from such simulations have already been used in Steidel et al. (1999), Adelberger & Steidel (2000), and Shapley et al. (2001); they are described in detail in Adelberger (2002). The simulations show that measurement errors tend to be dominated by the systematics of the photometry— detection, blending, etc.— and not by Poisson counting statistics of the fluctuations in the sky background as is often assumed for faint galaxy photometry (see Steidel & Hamilton 1993). The photometric uncertainties for detected objects depend in a complex way on local environment, seeing, depth, color, and magnitude. In Table 3, we summarize the typical photometric uncertainties associated with objects having the colors of LBG candidates (see discussion below). These were estimated by adding a large number of objects with colors and magnitudes similar to the LBGs of interest, and examining the photometric statistics of the objects that were recovered as LBG candidates. Note that the “input” colors and magnitudes need not have satisfied the LBG color selection criteria, and a considerable fraction of the objects with input

⁶The RMS values used for this calculation were corrected for pixel-to-pixel correlations introduced in the process of registering and re-sampling the data. Although high order interpolation schemes were used for the re-sampling, the actual measured values of σ_{sky} are too small by $\sim 10\%$.

“LBG” characteristics are not recovered, for a variety of reasons. Evaluating the photometric *completeness* as a function apparent magnitude and color is a separate, important question, particularly for using the photometrically-selected samples for inferring properties of the “parent population” – see Steidel et al. (1999) and Adelberger (2002) for more complete discussions of this topic and applications of the technique.

The data in Table 3 are an average over the fields included in the survey, and so indicate typical photometric uncertainties. Full modeling of these effects in each field is important for many applications of the data; here we simply make a few general points. First, it is often the case that the uncertainties in, e.g., $G - \mathcal{R}$ colors, are smaller than the errors in the \mathcal{R} magnitudes (which are almost independent of magnitude). This is because, to first order, the systematics that dominate the magnitude errors (crowding, local sky evaluation, blending) are strongly correlated in the G and \mathcal{R} passbands. Since we are using identical apertures (defined in the \mathcal{R} band) in each band, we suffer most from systematics in the detection phase, and then to a lesser extent in measuring colors. In addition to increased uncertainties due to these systematics, there are also *biases* that are introduced. Table 3 shows that, at the faint end of the LBG magnitude distribution, especially for objects with redder $G - \mathcal{R}$ colors, there is a tendency to measure galaxies to be systematically too red in $G - \mathcal{R}$ by up to ~ 0.1 magnitudes. This is related to the fact that the apertures are defined in the \mathcal{R} band, and adjust themselves to positive fluctuations in the sky background near the sky level. Since the same aperture is applied to the G band light, the aperture is not free to adjust itself similarly to maximize the G band light (see a more extensive discussion in Steidel & Hamilton 1993). Similar reasoning also explains the tendency to *over-estimate* slightly the \mathcal{R} band flux for the brightest objects, although this may also be due to the fact that larger isophotes are more likely to include light from neighboring objects that are not individually detected.

An estimate of the consistency of the photometry from field to field can be made by comparing the colors and number counts of faint objects detected in each. For this particular benchmark, we take all objects in the apparent magnitude range $22.5 \leq \mathcal{R} \leq 25.0$ in each field. This range was chosen to be sufficiently faint so as to minimize fluctuations in the foreground (low redshift) galaxy population and different stellar contamination as a function of Galactic latitude, but bright enough that incompleteness at the faint end (that is very seeing and depth dependent) is unlikely to be important. The statistics on the surface density and the mean $G - \mathcal{R}$ and $U_n - G$ colors (for objects significantly detected in all 3 bands) are summarized in Table 2. The surface density of objects in the $\mathcal{R} = 22.5 - 25.0$ range has an average of $\simeq 26$ arc min $^{-2}$ and a field-to-field scatter in the mean of $\sim 7\%$ (see Table 2). Not surprisingly, there is a tendency for fields with better seeing to have slightly higher surface densities, likely indicating differences in photometric completeness at the $\sim 10\%$ level (due to both increased depth and decreased blending) depending on the seeing. The slope of the \mathcal{R} band number counts (Steidel & Hamilton 1993) is such that a zeropoint error of 0.1 magnitudes would translate into a change in the surface density of 7%, so that at least some of the field-to-field scatter could be attributed to slightly different \mathcal{R} band photometric zero points. It is easy to imagine that uncertainties in the Galactic extinction could modulate the zero points by up to 0.05 magnitudes, particularly in fields with significant Galactic $100 \mu\text{m}$ cirrus emission.

The field-to-field scatter in the mean colors of the faint but well-detected objects used in the benchmark test is 0.04 magnitudes for $G - \mathcal{R}$ and 0.06 magnitudes for $U_n - G$. In most cases, the photometric calibration of each field is independent of the other fields (because it takes ~ 2 good nights to image a single field, generally only one field was observed per typical observing run) so that much of this scatter can be attributed to the uncertainty in the calibration of the photometric zero points. Additional scatter might result from uncertainties in the dependence of atmospheric absorption on airmass, differences in the spectral response of

the telescope plus detector system⁷, systematic differences in the calibrations of different spectrophotometric standard stars, and uncertainties in Galactic extinction (we note that $E(G - \mathcal{R}) = 1.4E(B - V)$ and $E(U_n - G) = 1.1E(B - V)$). Finally, of course, there can be a contribution to the field-to-field scatter in all of the quantities examined due to sample variance (i.e., “cosmic scatter”) that is difficult to quantify. In view of the many possible ways that the photometry might have been affected, one might conclude that it is actually surprisingly consistent from field to field. In any case, no measures have been taken to adjust the photometry in any field excepting SSA22b, whose G -band zero point was adjusted slightly to bring it into better agreement with its neighbor field, SSA22a (which had much more trustworthy calibration data). It may be important to keep in mind, for some applications, that systematic effects in both colors and magnitudes at the ~ 0.1 mag level are possibly present in the photometric catalogs.

4. PHOTOMETRIC SELECTION OF CANDIDATES

The selection of objects in color-color space for spectroscopic follow-up has been dictated by practical considerations and partially by expectations from simple models (which have been subsequently verified empirically). Our filter system was originally intended for the efficient selection of objects near $z \sim 3$ through its sensitivity to the Lyman continuum decrement passing through the near UV passband. The original criteria we used for flagging candidates (Steidel & Hamilton 1992, 1993; Steidel, Pettini, & Hamilton 1995) were designed to be conservative in the sense that the part of the $U_n G \mathcal{R}$ color space selected was deliberately steered well away from the stellar locus, and from the bulk of the so-called “faint blue galaxies” (e.g., Guhathakurta et al. 1990). Inspection of a simple diagram such as the one in Figure 2, which shows the expected colors versus redshift of model star-forming galaxies with a variety of assumed reddening by dust, makes it clear that a selected region is going to cut across any realistic galaxy distribution in a complex manner and that, in particular, the region of color space where the galaxy $U_n - G$ colors are increasing rapidly is likely to also mark galaxies at redshifts $z \gtrsim 2$. As discussed in Steidel et al. (1999), and to a greater extent in Adelberger (2002), color criteria will select a different subset of the star forming galaxy population as a function of redshift, but careful attention to completeness issues as a function of color, magnitude, and redshift can allow one to reconstruct the true distribution of the underlying “population” over the full range of intrinsic properties represented in the observed sample. The object of color selection is to select the maximum number of objects having the properties of interest with the minimal contamination from objects at other redshifts.

All the objects in our survey were chosen to satisfy the color criteria $G - \mathcal{R} \leq 1.2$, $(U_n - G) \geq (G - \mathcal{R}) + 1.0$, but for some purposes (mainly historical) we subdivided this region of color-color space into 2 regions, and in each we distinguish between objects which are and are not detected in the U_n band at the 1σ level. A summary of the selection criteria we have used for the survey discussed in this paper (results from surveys using other photometric selection criteria will be presented elsewhere) is given in Table 4, and these regions are illustrated on the two-color diagrams in Figures 2 and 3. The region occupied by the “C” and “D” candidates is identical to that proposed for “robust” candidates in Steidel, Pettini, & Hamilton 1995; initial spectroscopic success in expanding these criteria to smaller $U_n - G$ colors without introducing significant contamination from low-redshift objects prompted us to include the additional “strip” defined by the “M” and “MD” criteria. Including this smaller region, which in practice has a much higher “density” of candidates than the C/D

⁷We have seen clear evidence for large variations in the UV reflectivity of telescope mirrors depending on time since the last aluminization, or when the mirror has been subjected to accidental moisture condensation, etc.

region of color space, brings the surface density of candidates to an average of ~ 1.8 galaxies arcmin $^{-2}$ – well matched to the density required for making good use of the available multi-object spectroscopic capabilities at Keck. Evidently, based on more recent exploration of still bluer (in $U_n - G$) objects with the LRIS-B instrument, one could relax the criteria further still without paying a significant penalty by including many low-redshift interlopers. However, as we discuss further below, for our initial spectroscopic follow-up, the galaxies in the redshift range $2.7 \lesssim z \lesssim 3.4$ provide an almost ideal match to the spectroscopic capabilities that were available during the time that these survey data were obtained. Including lower redshift objects would have led to significantly higher rates of spectroscopic incompleteness.

One can see in figure 2 that some contamination by Galactic stars is expected in both the C/D and M/MD regions of the selected color regions. Over the magnitude range $19 \leq \mathcal{R} \leq 25.5$, the G and K stars will all be main sequence stars. We discuss the stellar contamination in §6 below.

Because of photometric errors and real color differences among selected objects at a given redshift, the act of drawing what are to some extent arbitrary lines in color space does not impose a hard redshift cutoff for the sample. Instead, the color cuts should be thought of as providing only crude control over the redshift selection function, while at the same time allowing for samples with a fairly broad range of intrinsic properties at a given redshift. This is a desired property if one is interested in the statistics of star forming galaxies in general and not those with a particular rest-frame properties. Since at the time we began this survey the $z > 2$ universe was largely unexplored, it seemed most prudent to simply “see what is there” rather than fine-tune the selection criteria based on (perhaps unfounded) expectations.

Still, small differences in photometry can have a significant effect on which objects fall into the selection region, particularly near the “boundaries” of the windows: for example, 0.1 mag differences can easily turn C/D objects into M/MD objects, and the same differences can cause significant numbers of objects which belong in the M/MD window to fall out of the observed sample. There are some fields in which our photometry evolved over time, either because deeper data were obtained or because significantly improved calibrations became available. For this reason, in some fields we have obtained spectra of a number of galaxies that were candidates in a previous incarnation of the photometry, but no longer are included in the “official” selection windows. These objects, when redshifts were successfully measured, will be included for completeness’ sake in the LBG catalogs below, but are designated as “old” (e.g., HDF-oMD49) and have not been used in any statistical calculations in this paper.

5. SPECTROSCOPIC OBSERVATIONS AND DATA

After the initial spectroscopic tests of the Lyman break technique (see, e.g., Steidel et al. 1996a), we converged on a general approach that was followed for all subsequent spectroscopy. Having generated lists of photometric candidates as discussed in the previous section, the candidates were visually inspected to exclude obviously spurious objects (e.g., “objects” associated with asteroid trails, diffraction spikes, bleed trails, etc.) and these objects were deleted from the lists. Each object was assigned a numerical priority, based primarily on apparent magnitude in the “blank” fields, and on a combination of apparent magnitude and projected distance from the background QSOs in the fields observed as part of the galaxy/IGM survey described in Adelberger et al. (2003). Occasionally objects of particular interest would receive especially high priorities to make sure they would be assigned to a slit mask, but in general objects brighter than $\mathcal{R} = 25$ were given roughly two times higher priority than those fainter than $\mathcal{R} = 25$, and “C” and “D” type candidates were given higher priorities than “M” and “MD” candidates. A comparison of the apparent \mathcal{R}

and G magnitude distributions of objects for which spectroscopy was attempted versus the full photometric sample is shown in Figures 4 and 5, respectively. Figure 6 shows similar distributions separated into the the C/D/M/MD subsamples.

Slit masks were designed by allowing a computer program to maximize the total priority of the objects that could be placed on a given slit mask. Usually sky position angle and mask center position were allowed to vary in the optimization process. The program allowed slits to be placed anywhere within a field 7.3 by 5 arc minutes so long as they did not overlap in the spatial direction. The minimum acceptable slit length was $\sim 9''$ to allow for adequate sky subtraction for even the shortest slits. Once an object was selected for a mask, its priority was downgraded (or in some cases it was removed completely) before designing the next mask for a given field. A typical slit mask included an average of 15–20 $z \sim 3$ LBG candidates. Often we would experiment with “filler” objects selected using different color criteria to fill in any gaps in the slit mask (~ 10 – 15 additional slits per mask). In this way we were able to explore how the use of different color criteria would influence the resulting sample. In this paper, we report the results only for objects satisfying the color criteria described in §4. Our method for choosing objects for spectroscopy tended to favor sparse ($\sim 50\%$) sampling of the full imaged region over complete spectroscopy in any given region. Examples of the spatial distribution of objects targeted for spectroscopy versus the full distribution of candidates are shown in Figure 7.

All but a few of the slit masks observed for the $z \sim 3$ LBG survey used the same instrumental configuration. We used the Low Resolution Imaging Spectrometer (LRIS; Oke et al. 1995) on both Keck I (October 1995–August 1996 and January 2000–present) and Keck II (October 1996–November 1999). We used a 300 line mm^{-1} grating blazed at 5000 Å in first order, leading to a dispersion of 2.47 Å/pixel on the Tektronix 2K×2K CCD and a typical spectral coverage that was adjusted (with the grating tilt) to include at least the 4000 – 7000 Å range on every slit. The nominal spectral resolution in combination with the $1''.4$ slitlets⁸ is ~ 12.5 Å (FWHM) evaluated from the width of night sky emission lines. However, given that most of the galaxies are barely resolved even in good seeing, the actual spectral resolution is “seeing-limited” in almost all cases. The typical image quality at the detector was ~ 0.8 – $0.9''$ (FWHM), so that the effective spectral resolution (neglecting guiding errors) is closer to 7.5 Å in most cases. No attempt was made to observe masks with position angles close to the parallactic angle, and we sometimes observed masks to airmasses of 1.5–1.6 when fields were setting. Thus, there is some danger that the apparent object position perpendicular to the slit could be wavelength dependent particularly when the seeing was very good.

A small subset of the data in the Q0933+288 and Q1422+2309 fields, and all of the data in Q0302-003, were obtained using the new blue arm (LRIS-B; McCarthy et al 1998, Steidel et al. 2003, in preparation) of LRIS between late 2000 and early 2002. Most of these observations were obtained by directing all of the incident light into the blue channel using a mirror in place of the usual dichroic beam-splitter. The disperser was a 300 lines mm^{-1} grism blazed at 5000 Å providing a typical wavelength coverage of 3500–7500 Å for each slitlet. The spectral resolution is slightly higher than that of the LRIS-R data, while the spectral throughput is significantly higher. During the time these LRIS-B data were obtained, the detector was an engineering grade Tektronix 2k x 2k UV/AR coated CCD.

The observations for each slit mask were obtained in a series of 1800s exposures. The telescope was dithered slightly (~ 1 – $2''$) in the slit direction between exposures in order to sample different parts of the detector and to allow for a variety of options for subtracting the sky background. Initially, we obtained

⁸These were considerably wider than the typical seeing at the Keck Observatory, and were chosen to mitigate the effects of atmospheric dispersion and errors in the relative astrometry. With hindsight they were probably wider than they needed to be.

total integration times of 2 – 3 hours per mask, but we found that under good observing conditions (seeing $\text{FWHM} < 0.8''$, clear) we could easily obtain adequate data in a total integration time of 5400s. Flat fields were obtained at the end of the observing sequence of a given mask using a halogen lamp internal to the spectrograph. An observation of internal arc lamps (Hg, Ne, Ar, Kr, Xe) was also obtained at the end of the observing sequence for a given mask.

The data were reduced using a custom package based on IRAF scripts. Each observation of a given slit mask was “cut up” into individual spectrograms and flat-fielded using the appropriate (continuum-normalized) image section of the flat-field image. Cosmic ray identification was done using a routine that identifies cosmic ray hits morphologically and adds them to a mask that is maintained for each exposure and for each slitlet’s spectrogram. The background was subtracted by fitting a polynomial at each dispersion point whose order was varied depending on the length of the slitlet (the slitlets varied in length from $\sim 9''$ to $\sim 20''$). The two-dimensional, background-subtracted spectrograms were then shifted into registration using the positions of night sky emission lines in the spectral direction (to remove the effects of any flexure during the 1.5-2.5 hours a given field was being observed) and object continuum positions in the spatial direction, and averaged. Pixels that had been masked as cosmic ray hits were excluded in forming the final stacked spectrograms. The arcs corresponding to each slitlet were reduced in exactly the same way as the data (excepting the background subtraction). The final one-dimensional spectra were then traced and extracted from the background-subtracted final stacks; one-dimensional arc spectra were extracted from the same regions. The wavelength solutions were then obtained by fitting a 5th-order polynomial to the arc lamp spectra; typical residuals were $\sim 0.2\text{\AA}$. Finally, each 1-D spectrum was extinction corrected and (approximately) flux calibrated using observations of spectrophotometric standards observed with a $1''.5$ long slit and the same 300/5000 grating used for the slit masks, and then reduced to vacuum wavelengths to facilitate redshift measurement using far-UV transitions.

5.1. Spectral Identification

As has been discussed extensively elsewhere (e.g., Steidel et al. 1996a, Steidel et al. 1998, Pettini et al. 2000, 2001), most of the easily identifiable features in LBG spectra are interstellar absorption lines of very strong transitions in the 1200 – 1700 \AA range in the rest frame. The dark sky background (and high instrumental efficiency) in the 4000 – 6500 \AA range and the typical 5-10 \AA equivalent widths of a number of easily recognizable absorption features makes it surprisingly easy to measure redshifts even from spectra having a signal-to-noise ratio (S/N) per resolution element of only a few. The process is also greatly assisted by the nature of these absorption features. As described in detail in Shapley et al. 2003, objects with the strongest Lyman α emission lines tend to have weaker interstellar absorption features (and bluer continua) while objects having weak Lyman α in emission or Lyman α completely in absorption tend to have significantly stronger interstellar absorption lines.

The spectra for the LBG sample span a large range in quality, from objects with single emission line detections to those with many identified absorption lines. Here we outline the criteria for assigning redshifts from the spectra. Every observed spectrum was examined interactively (in both 1-D and 2-D) by at least two of us; the same two people examined the whole sample several times each. Approximate redshifts were first assigned by identifying a single feature and marking the expected positions of other strong far-UV features. More precise redshifts were then measured; in the case of Lyman α emission lines by fitting a Gaussian to the observed profile, while for absorption features the average redshift given by the centroid positions of all well-detected features was adopted. If a single emission line was observed, especially in combination with

a discernible continuum drop shortward of the line, the redshift was considered secure. In general, a single emission line is insufficient to reliably identify spectra, but in combination with the photometric break that placed the object into the sample, a single emission line is extremely unlikely to be anything except Lyman α , particularly if that line suggests a redshift consistent with the continuum break.

The spectra generally fall into 3 fairly distinct classes: those that are identified using Lyman α emission and broad continuum properties alone, those that are identified by means of multiple interstellar absorption lines, and those that have both Ly α emission and one or more clearly identified absorption lines. Examples of each type are shown in Figure 8; these spectra were chosen also to be representative of the range of quality present in the full sample. The precision with which the redshifts are measured, based upon independent measurements of the same spectra or on the scatter among different lines, is $\Delta z \simeq 0.002$ for absorption line measurements and $\Delta z \simeq 0.001$ for emission line objects. The larger dispersion for the absorption line objects reflects the fact that these lines are often quite broad compared to the emission lines and have lower S/N. As has been discussed extensively elsewhere (e.g., Franx et al. 1997; Steidel et al. 1998; Pettini et al. 1998, 2000, 2001, 2002; Adelberger et al. 2003; Shapley et al. 2003) the Ly α emission and interstellar absorption features are almost universally separated by at least several hundred km s^{-1} . This phenomenon is generally interpreted as evidence for strong outflows from LBGs, where the interstellar absorption lines are produced by the near side of the outflow, and the Ly α emission line by the back-scattering from the opposite side of the outflow, and where the true systemic redshift of the galaxy lies somewhere in between. For this reason, we have recorded both emission (z_{em}) and absorption (z_{abs}) redshifts for each galaxy, when both have been measured. Methods for obtaining more precise systemic redshifts from the far-UV spectra alone (and the resulting uncertainties) are discussed in Adelberger et al. (2003).

Table 5 summarizes the total number of objects observed in each of the 17 fields. The overall spectroscopic success rate is $\sim 76\%$ (including 3.5% spectroscopically identified interlopers); most of the 24% of failed measurements were obtained under less than ideal conditions, whereas masks obtained under good or very good observing conditions (clear skies, seeing $\text{FWHM} \leq 0.8''$) tended to reach greater than 90% success, where success is defined as the fraction of attempted objects that have yielded redshifts. Note that in figure 4, the spectroscopic success rate actually reaches a minimum in the $\mathcal{R} = 24.5 - 25$ range, and then *increases* toward fainter magnitudes beyond $\mathcal{R} \sim 25$. While somewhat counter-intuitive, it is due to the nature of our photometric selection criteria. For the faintest objects in the sample, the demands of minimum “spectral curvature” criteria (i.e., the difference between the $U_n - G$ and $G - \mathcal{R}$ color) impose significant dynamic range constraints at the faint end of the apparent magnitude range considered. Only the bluest objects at $\mathcal{R} = 25.5$ can be selected using our color criteria because of the finite depth of the U_n band images. The bluest LBGs almost invariably have Lyman α in emission, so that redshifts are usually measurable even when there is little or no (spectroscopically) detected continuum. The relationship between color and spectral properties is discussed in much more detail in Shapley et al. (2003). Figure 9 shows composite spectra formed from each quartile of the spectroscopic sample divided by the equivalent width of the Lyman α feature. A detailed discussion of the astrophysics that can be extracted from these and other LBG composite spectra is contained in Shapley et al. 2003.

In some cases, the quality of the observed spectrum is inadequate to assign what we consider to be a precise redshift, but is good enough for a reasonably secure one. Usually these spectra are of high enough quality to note the position of a “break” in the continuum that lies near the wavelength of Lyman α (caused by the blanketing of the Lyman α forest) and where 1 or more other (low S/N) plausible spectral features can be identified, but where none of the additional features is secure enough to provide a very high degree of confidence. Experience with repeat observations of insecure redshifts suggests that about 80% of them

are very accurate, with the remainder being incorrect by as much as $\Delta z \sim 0.1$. We have attempted to use cross-correlation techniques to improve on the redshift identifications of redshift failures or insecure redshifts but have found that the results lead to an unacceptable incidence of spurious identifications; thus, we have decided to err on the side of caution. Objects with less certain redshifts have been flagged in the catalog tables (with redshift entries preceded by a colon, e.g. “:2.789” in tables 7–23), and are not used in any analyses that depend on precise redshift measurements. Of the total of 955 objects satisfying the LBG photometric criteria with spectroscopic redshifts $z > 2$, 121 fall into this less precise category. There is no significant difference in the overall redshift distribution of the 834 class 1 redshifts compared to the 121 in class 2.

A redshift histogram for the full spectroscopic sample is shown in figure 10. Also shown are the separate histograms for the 4 “types” of LBG candidates, to illustrate overall redshift differences depending on the location in the color-color plane of the candidates. The redshift statistics are summarized in table 6. The general trends with color can be understood as follows (see figure 2 for a graphical depiction): objects of a given intrinsic spectral energy distribution (SED) will become redder in both $G - \mathcal{R}$ and $U_n - G$ with increasing redshift over the range spanned by the survey. The $G - \mathcal{R}$ effect is due to increased blanketing of the G passband by the Lyman α forest, and the $U_n - G$ effect is caused by an increasingly large fraction of the U_n passband falling shortward of the rest frame Lyman limit (for $z > 3.3$ the U_n passband is entirely shortward of this rest wavelength). Because of the finite depth of the U_n images, we normally cannot measure a $U_n - \mathcal{R}$ color greater than about 3 magnitudes at the faint end of the \mathcal{R} magnitude distribution. The limits on $U_n - G$ color will then clearly depend on the measured $G - \mathcal{R}$ color. The slightly higher redshifts of “C” type candidates compared to “D” objects, which differ only in whether they are detected at better than the 1σ level in U_n (see §3 and table 2), are best understood as being due to the very strong redshift dependence of the $U_n - G$ color. As expected (see Figure 2), the “MD” type objects lie at somewhat lower redshifts on average than the “C” and “D” type candidates—the U_n band is less absorbed by the IGM and the Lyman limit at smaller redshifts. The “M” type candidates, which are objects with less stringent constraints on the spectral curvature (measured by the difference between $U_n - G$ and $G - \mathcal{R}$ color) are at *higher* redshift than even the “C” candidates. This is most likely due to the dynamic range problem mentioned above; “M” candidates tend to be objects that are too red in $G - \mathcal{R}$ to result in stringent limits on $U_n - G$, evidently driven mostly by the fact that they lie at higher redshifts where the red color is due primarily to forest blanketing. The LBG selection function, formed by the sum of all of the candidate types, reflects the overall sensitivity of the survey to galaxies as a function of redshift. We emphasize that the shape of the LBG selection function is to some extent dictated by the sampling rate of the $U_n G \mathcal{R}$ color plane which, as we have discussed, favored (by fraction) objects with larger limits on or measurements of the $U_n - G$ color. Table 6 summarizes the sampling and success rates for the various candidate types; from this, it can be seen that C/D candidates enjoyed a selection rate approximately 50% higher than M/MD candidates, and had a spectroscopic success rate that was slightly higher as well. Proper accounting of both the photometric biases and the spectroscopic sampling rate is necessary for many applications of the LBG sample (see, Adelberger & Steidel 2000, Steidel et al. 1999, Shapley et al. 2003).

5.2. Field Redshift Distributions

Figure 11 shows redshift histograms for each of the 14 distinct sky regions surveyed. Here we have combined fields with two adjacent pointings (DSF2237a,b; SSA22a,b; CDFa,b) into single histograms. In each panel, the light colored histogram shows the expected redshift distribution given the overall survey

selection function; thus, the figure illustrates qualitatively the clustering properties within individual fields and the variance of the large-scale redshift distribution from field to field. Because some of the fields were selected to surround known QSOs or AGN (Q0302–003, Q0201+1120, Q0256–000, Q0933+289, B20902+34, Q1422+2309, and Q2233+1341), we have marked the redshift of the known objects in each case.

Table 5 summarizes the spectroscopic results in each of the 17 fields, including the fraction of candidates that were spectroscopically observed, the fraction yielding redshifts $z > 2$, and the fraction of “interlopers” or contaminants.

6. CONTAMINATION OF THE LBG SAMPLE

A total of 40 stars are spectroscopically identified in the full LBG sample, or $\sim 4\%$ of the total spectroscopic sample. The colors and spectra of these stars (see figures 2, 3) suggest that most are Galactic K sub-dwarfs (i.e., halo main sequence stars). In figure 12, we plot the histogram of observed stars as a function of apparent \mathcal{R} magnitude. As can be seen from the figure, the stellar number counts are essentially flat from $\mathcal{R} = 22$ to $\mathcal{R} = 24$, but then exhibit an apparent cut-off fainter than $\mathcal{R} \sim 24.0 - 24.5$. There is essentially no identified stellar contamination of the LBG sample fainter than $\mathcal{R} = 24.5$; however, we caution that the spectra of very faint stars may be more difficult to identify than LBGs of the same apparent \mathcal{R} magnitude, since there are generally fewer strong features in the stellar spectra. Stars are also somewhat *under-represented* for objects brighter than $\mathcal{R} \sim 23$, since when objects were obviously stellar *and* had colors on the stellar locus, they were given lower weights than other objects of the same apparent \mathcal{R} magnitude (this effect can be seen in Figure 6 as a smaller fraction of spectroscopically observed objects in the brightest bins for “MD” type candidates; the “MD” region of color-color space contains most of the stellar interlopers, as shown in Figure 3).

Of the 955 objects with redshifts $z > 2$ and $\mathcal{R} \leq 25.5$ in the sample satisfying the LBG color criteria 28 (3%) have obvious signatures of AGN in their spectra. The AGN sub-sample is certainly interesting in its own right, and is discussed in more detail in Steidel et al. (2002); here we discuss it only as a source of contamination of the LBG sample. All AGN or QSOs that were known prior to the survey and which were deliberately placed within the field of view have been excluded from any numbers quoted below (i.e., the primary QSOs in the QSO fields, and the radio galaxy B20902+34, are excluded).

Of the 9 objects with $z > 2$ and $\mathcal{R} \leq 23$, 7 are identified as either broad or narrow-lined AGN, while AGN comprise 8 of 31 high redshift objects (i.e., non-stars) brighter than $\mathcal{R} = 23.5$. Thus, as for the stars, the AGN contamination fraction is highly magnitude dependent. AGN have generally been excluded from any published statistics of LBGs (e.g., clustering, luminosity functions, etc.), although we have shown in Steidel et al. (2002) that the AGN in the sample are plausibly hosted by objects similar to Lyman break galaxies.

Aside from the 40 stars, there are only 5 other identified objects in the spectroscopic sample having $z < 2$, two of which have $z \simeq 1.99$. The other 3 “interlopers” all have $z \sim 0.5$, and all three are in the “less secure” class of redshift. The very low $z \leq 2$ interloper fraction can be attributed to a relatively conservative color selection window, and to some extent may be caused by the limited spectral coverage of the typical survey spectrum, which would generally have had difficulty identifying galaxies having $0.9 \gtrsim z \lesssim 2.1$. However, we believe that most of the identification failures have redshifts consistent with the LBG selection function but failed because of inadequate S/N, in the majority of cases due to relatively poor observing conditions. As discussed above, the primary basis for this belief is that the masks observed under the best conditions often

achieved better than 90% spectroscopic success rate, whereas there were many poor masks on which only a few of the brightest galaxies were identified; it was often impossible to re-observe objects that happened to be assigned to poorly-observed masks.

7. NOTES ON INDIVIDUAL FIELDS

In the interest of completeness, we have included results for all of the survey fields observed during the course of the $z \sim 3$ Lyman break survey. While the intended uses of the survey fields has varied, the same selection criteria and general survey approach were used for all 17 fields. Several of the survey fields are “blank” fields chosen either because other surveys had been or will be conducted there (e.g., Westphal, HDF-N, CDFa) or as specially selected fields at particular RA that would be accessible during scheduled observing runs with minimal Galactic extinction and very bright stars (e.g., DSF2237a and DSF2237b). Several other fields are pointings adjacent to initial survey fields, chosen to increase the angular extent beyond the $9'$ fields afforded by the Palomar prime focus imager COSMIC (SSA22b, DSF2237b, CDFb). In all cases we have treated these additional, adjacent fields independently, since both the imaging and spectroscopic data were generally obtained on different observing runs and as a result the data had somewhat different seeing, exposure times, and depth depending on the observing conditions and available observing time. Five of the fields were centered on background QSOs suitable for high resolution spectroscopy to be used in a comparison of the galaxy distribution with the IGM along the same line of sight (Q0256–000, Q0302–003, Q0933+289, Q1422+2309, Q2233+1341), some of the results of which are presented elsewhere (Adelberger et al. 2003). Three of the fields (Q0000–263, 3C324, Q0201+1120) are included here but have generally not been used as part of statistical studies either because of their small size (in the case of 3C324 and Q0000–263) or because of excessive Galactic extinction (in the case of Q0201+1120). More details on each field are given below; see also Tables 1, 2, and 6.

Tables 7-23 contain the complete catalogs for all 17 of the survey fields. Entries of -1.000 in the redshift column indicate that a candidate has never been attempted spectroscopically; -2.000 in both the z_{em} and z_{abs} columns indicates that the object has been observed spectroscopically but no reliable redshift resulted. Objects whose redshift measurement depended only on emission lines (usually Lyman α only, for all but the AGN) have a -2.000 in the z_{abs} column, and those objects without measurable emission lines have -2.000 in the z_{em} column. Redshift entries preceded by colons indicate that the measurement is uncertain, as discussed in §5.1. The distinction between objects that are “detected” in the U_n band and those that were assigned a $+1\sigma$ limit is not made in the table entries; we refer the reader to Table 4 for a summary of the way in which the tabulated $U_n - G$ color should be interpreted, depending on the candidate type. The significance of a particular $U_n - G$ color measurement can be judged by comparing the U_n magnitude [i.e., $\mathcal{R} + (G - \mathcal{R}) + (U_n - G)$] to the tabulated values of $\sigma(U_n)$ listed in Table 2 for each field. Most of the $U_n - G$ values, being either limits or close to limits, are uncertain by $0.4 - 0.6$ magnitudes, depending on color and apparent \mathcal{R} magnitude.

7.1. Q0000–263

The field of this $z_{em} = 4.10$ QSO was included in pilot studies of LBG search techniques (Steidel & Hamilton 1992, 1993). These data were obtained subsequently at the ESO NTT in order to improve significantly on the depth and seeing of the original data obtained at CTIO. The complete catalog of LBGs

in this field is given in Table 7. Some of the spectroscopic results in this field were presented in Steidel et al. 1996a—the designation of the candidates has since changed, but cross-references to the old names are given in the table. One note of caution is that the G and \mathcal{R} filters used for the NTT data are somewhat different in both center wavelength and bandpass from the filters used for the rest of the fields; as a result, the photometry and candidate selection is expected to have slightly different systematics compared to other fields in the survey. The Q0000–263 field has generally not been used for more recent statistical studies of LBGs.

The object Q0000-C7 (see Table 7) is the emission line galaxy “G2” discovered via narrow-band Lyman α imaging by Macchetto et al. 1993 and further discussed by Giavalisco et al. 1994, 1995.

7.2. CDFa,b

CDFa is centered on the “Caltech 0 Hour Redshift Survey Field” discussed by Cohen et al. 1996, which itself is centered on a relatively deep HST/WFPC-2 pointing. CDFb is an adjacent field to the South (and slightly to the East to avoid a bright star). The complete LBG catalogs for these fields are presented in tables 8 and 9.

7.3. Q0201+1120

The data obtained in this field were discussed by Ellison et al. (2001), which presented results on the $z = 3.390$ damped Lyman α system in the spectrum of the $z = 3.605$ QSO. It became clear to us after the imaging data were obtained that the field suffers from quite heavy Galactic extinction (amounting to ~ 0.7 mag in the U_n band—see Table 2), although the photometry, after nominal correction for extinction, appears to agree well with that in other fields. Nevertheless, we have not used Q0201+1120 for statistical studies of LBGs due to lingering uncertainties about the quality of the photometry and the high probability of patchy (i.e., strongly variable) extinction over the field. Table 10 contains the LBG catalog for this field.

7.4. Q0256–000

The field is centered on the $G = 18$ QSO with $z_{em} = 3.364$, and was observed as part of a survey to compare distribution of C IV and H I in the IGM to the galaxy distribution in the surrounding volume (Adelberger et al. 2003). The LBG data are summarized in Table 11.

7.5. Q0302–003

Another field observed as part of the galaxy/IGM survey, the QSO ($z_{em} = 3.281$) is also one of the few lines of sight that has been observed in the far-UV to probe the re-ionization of He II near $z \sim 3$ (Heap et al. 2000). While a $15'$ region was observed photometrically, only a $\sim 7'$ region in the vicinity of the QSO has been observed spectroscopically to date. The data in this paper include only the region covered spectroscopically, although full photometric catalogs are available on request. Table 12 provides the catalog over the spectroscopically observed region.

7.6. B20902+34

This field is centered on the famous $z = 3.392$ radio galaxy B20902+34 (Lilly 1988; the radio galaxy is itself a LBG candidate, object B20902-D6 in Table 13). It was observed to investigate the density of LBGs around a high redshift radio galaxy, given the conventional wisdom that radio galaxies inhabit rich environments. As can be seen from Figure 11, there is not a highly significant galaxy over-density at the redshift of the radio galaxy, although the statistics are not very constraining given the relatively small number of spectroscopic redshifts in the field and the fact that the LBG selection function is rapidly declining at $z \sim 3.4$. The photometric data in this field are a combination of data obtained at the William Herschel telescope prime focus imager and the P200+COSMIC at Palomar; the field size is limited by the scale of the WHT imager at the time the data were obtained.

7.7. Q0933+2854

This field was selected because of its low galactic extinction and the presence of the $z_{em} = 3.428$, $G = 17.5$ QSO, making it ideal for the galaxy/IGM survey project. The photometric data are a combination of KPNO 4m+Mosaic Camera data and data from the Palomar 5m+COSMIC system; the region presented in this paper is the region common to the two data sets, limited by the size of the COSMIC field. The LBG catalog is presented in Table 14.

7.8. HDF-N

We confine the data set for this paper to objects that were identified only on the basis of the ground-based imaging from the Palomar 5m+COSMIC, and not on other high redshift objects identified on the basis of the deep WFPC-2 imaging near the center of the $8'.7$ field (cf. Steidel et al. 1996b, Lowenthal et al. 1997; Dickinson 1998). Where there is overlap between the HST-identified LBGs and the ground-based LBG survey we have provided a cross-reference in Table 15. The imaging data in the HDF-N were obtained under highly variable conditions, and hence are among the lowest-quality data in the survey (e.g., the U_n image is the shallowest of any of the 17 fields—see Table 2).

The X-ray properties of the (ground-based) LBGs in this field have been discussed by Nandra et al. (2002).

7.9. Westphal

This field is named after James Westphal, the PI for the HST/WFPC-2 observation of the deepest pointing of the “Groth Strip” WFPC-2 mosaic. The $15'$ field includes the north-east section of the Groth strip mosaic, and also several other relatively deep pointings of WFPC-2. This field contains the largest number of spectroscopically confirmed LBGs in the survey (188), and the highest level of spectroscopic completeness (relative to the photometric sample) of any of the “blank” fields. The field contains the entire Canada-France Redshift Survey (Lilly et al. 1996) 14 hour field, and will be the subject of a number of current and future deep observations at other wavelengths, including Chandra X-ray Observatory (200ks) and the Space Infrared Telescope Facility (SIRTF). The LBG catalog is presented in Table 16.

7.10. Q1422+2309

This field was chosen for the galaxy/IGM project, and is centered on the gravitationally-lensed $z_{em} = 3.620$ QSO ($G = 16.5$). We intended to obtain especially deep photometric data in this field because the spectra of the QSO are exceptionally good (it is perhaps the most-observed high redshift QSO in the sky). Pristine observing conditions at the William Herschel Telescope coupled with an EEV/Marconi CCD that provided high UV quantum efficiency allowed us to reach about 1 magnitude deeper in the U_n band than in any of our other fields. Hence, we were able to extend our selection criteria for LBGs to $\mathcal{R} = 26$ rather than our usual limit $\mathcal{R} = 25.5$. In addition to the 453 LBG candidates identified in this field, we also discovered a new $z_{em} = 3.629$, $\mathcal{R} = 22$ QSO only $40''$ from Q1422+2309 itself. This object, dubbed Q1422+2309b, is included in table 17 despite the fact that it does not quite satisfy the LBG selection criteria (it is slightly too red in $G - \mathcal{R}$).

7.11. 3C 324

Only one slit mask was observed in this field, but it is included for completeness. It was originally observed to coincide with a very deep HST/WFPC-2 observation of the radio galaxy field, but the positions of very bright stars forced moving the pointing to the extent that the overlap with HST is now rather small. The LBG catalog is presented in table 18.

7.12. SSA22a,b

The SSA22a field was originally chosen to include several HST/WFPC-2 pointings obtained as part of the Hawaii Deep Survey (e.g., Lilly, Cowie, & Gardner 1991; Songaila et al. 1994) and the Canada-France Redshift Survey (Lilly et al. 1996). Some results from LBG observations in this field were presented in Steidel et al. 1996a; in addition, a prominent redshift “spike” at $z = 3.09$, interpreted as a proto-cluster region, was analyzed by Steidel et al. 1998, and followed up with very deep narrow band imaging, reported in Steidel et al. (2000). Sub-mm follow-up of the field is described in Chapman et al. (2001). The candidate designations in SSA22a have changed compared to their original designations in these earlier papers; cross-references to the old names are given in table 19.

SSA22b is $8.5'$ south of SSA22a, and was observed to increase the transverse scale of the field to $\sim 9 \times 18'$. There are no HST pointings within SSA22b. The LBG catalog is presented in table 20.

7.13. DSF2237a,b

These fields were chosen because the best observing conditions at Palomar generally occur in August and September. The fields were chosen to be in a region of relatively low Galactic extinction, at high enough declination to be efficiently observed from both Palomar and Mauna Kea, and without stars bright enough to cause scattered light problems. There are no ancillary observations of these fields using other instruments or at other wavelengths, to our knowledge. DSF2237b is placed $8.7'$ due west of DSF2237a, to create a $\sim 9 \times 18'$ field. The LBG catalogs for the two fields are presented in tables 21 and 22.

7.14. Q2233+1341

This field is centered on the $z = 3.210$, $\mathcal{R} \sim 18.5$ QSO, and was observed as part of the $z \sim 3$ galaxy/IGM survey. The LBG catalog is presented in table 23.

8. SUMMARY AND DISCUSSION

We have presented the basic photometric and spectroscopic data for a large spectroscopic survey of color-selected objects near $z \sim 3$. The sample was constructed using very deep images in 3 passbands (U_n , G , and \mathcal{R}) in 17 different fields, covering a total solid angle of 0.38 square degrees. The color selection criteria were designed to isolate a well-defined redshift range for objects whose intrinsic spectral energy distributions are relatively blue in the rest-frame wavelength range $1200 \lesssim \lambda \lesssim 1700$, so that the marked discontinuity near the rest frame Lyman limit of hydrogen can be recognized using broad-band photometry.

Of the 2347 LBG candidates to $\mathcal{R} = 25.5$ satisfying the color selection criteria, 55% have been observed spectroscopically using LRIS on the Keck telescopes; of these, 76% have been spectroscopically identified and 73% have measured $z > 2$. The redshift distribution of the sample is approximately Gaussian, with $z = 2.96 \pm 0.29$. Approximately 4% of the identified objects are Galactic stars, while $\sim 3\%$ have obvious spectral signatures of AGN (broad or narrow high ionization emission lines) and have a redshift distribution consistent with that of the star-forming galaxies.

We provide a full catalog of the 2347 LBG candidates (plus additional candidates to $\mathcal{R} = 26$ in one field), including coordinates, photometry and, for those followed up spectroscopically, redshifts. Such data may be useful for future statistical studies of this population of high redshift galaxies.

This $z \sim 3$ survey for LBGs is one example of the type of approach to galaxy redshift surveys that is necessary for efficiently studying the high redshift universe. We estimate that the use of photometric pre-selection has improved the efficiency of studying galaxies near $z \sim 3$ by approximately a factor of 30 as compared to a traditional apparent magnitude selected survey to the same apparent magnitude limit. With similar approaches, using new wide-field imaging spectrographs coming on line on 8m-class telescopes, it would be within the bounds of reason to undertake surveys of the high redshift universe as ambitious as state-of-the-art surveys of local galaxies (e.g., 2DF and Sloan Digital Sky Survey). It is also feasible to use suitably designed photometric pre-selection for other redshift slices that will allow statistical samples of galaxies, isolating particular cosmic epochs, to be assembled rapidly. The obvious *caveat* is that these surveys cannot possibly take in all galaxies present at a particular redshift, and so they cannot be treated as all-encompassing; however, the same might be said of any survey. Insight into the process of galaxy formation and the development of large scale structure comes from making optimum use of available information and understanding how apparently disparate observations are related. The type of survey described above offers a large amount of statistical information that is relatively easily obtained using existing observational facilities, and may help guide future work as facilities and understanding improve.

We thank Melinda Kellogg, Matthew Hunt, and Dawn Erb for help with some of the data presented. CCS, KLA, and AES have been supported by grants AST-9596299 and AST-0070773 from the U.S. National Science Foundation and by the David and Lucile Packard Foundation. KLA acknowledges support from the Harvard Society of Fellows. We are especially grateful to the staffs of the Palomar Observatory, the Kitt Peak National Observatory, the William Herschel Telescope, and the W.M. Keck Observatory for assistance

with the observations. We benefited significantly from software developed by Judy Cohen, Drew Phillips, Patrick Shopbell, and Todd Small. We thank the entire team responsible for the Low Resolution Imaging Spectrometer, the instrument that has made this work possible. We wish to extend special thanks to those of Hawaiian ancestry on whose sacred mountain we are privileged to be guests. Without their generous hospitality, many of the observations presented herein would not have been possible.

REFERENCES

- Adelberger, K.L. 2002, Ph.D. thesis, California Institute of Technology
- Adelberger, K.L. 2000, in *Clustering at High Redshift*, ASP Conference Series Vol 200, eds. O. Le Fèvre, A. Mazure, & V. Le Brun (San Francisco: ASP), 13
- Adelberger, K.L., Steidel, C.C., Shapley, A.E., & Pettini, M. 2003, *ApJ*, in press
- Adelberger, K.L., & Steidel, C.C. 2000, *ApJ*, 544, 218
- Adelberger, K.L., Steidel, C.C., Giavalisco, M., Dickinson, M., Pettini, M., & Kellogg, M. 1998, *ApJ*, 505, 18
- Barger, A.J., Cowie, L.L., & Sanders, D. 1999, *ApJ*, 518, 5
- Bergeron, J., & Boissé, P. 1991, *A&A*, 243,344
- Calzetti, D., Armus, L., Bohlin, R.C., Kinney, A.L., Koornneef, J., & Storchi-Bergmann, T. 2000, *ApJ*, 533, 682
- Chapman, S.C., Lewis, G.F., Scott, D., Richards, E., Borys, C., Steidel, C.C., Adelberger, K.L., Shapley, A.E. 2001, *ApJ*, 548, L17
- Chapman, S.C., Scott, D., Steidel, C.C., Borys, C., Halpern, M., et al 2000, *MNRAS*, 319, 318
- Cohen, J.G., Cowie, L.L., Hogg, D.W., Songaila, A., & Blandford, R. 1996, *ApJ*, 471,5
- Cowie, L.L., Songaila, A., Hu, E.M., & Cohen, J.G. 1996, *AJ*, 112, 839
- Cowie, L.L., Lilly, S.J., Gardner, J.P., & McLean, I.S. 1988, *ApJ*, 332, 29
- Daddi, E., Cimatti, A., Broadhurst, T., Renzini, A., Zamorani, G., Mignoli, M., et al 2002; *A&A*, 384, L1
- Davis, M., Newman, J.A., Faber, S.M., & Phillips, A.C. 2001, in *Deep Fields*, (Springer), eds. S. Cristiani, A. Renzini, R.E. Williams, p. 241
- Dickinson, M. 2000, *Phil. Trans. RAS*, 358, 2001
- Dickinson, M. 1998, *STScI May Symposium Ser. 11*, (New York: Cambridge), p. 219
- Eggen, O.J., Lynden-Bell, D., & Sandage, A.R. 1962, *ApJ*, 136, 748
- Ellis, R.S., Colless, M., Broadhurst, T., Heyl, J., & Glazebrook, K. 1996, *MNRAS*, 280, 235
- Ellison, S.L., Pettini, M., Steidel, C.C., & Shapley, A.E. 2001, *ApJ*, 549, 770
- Franx, M., Illingworth, G.D., Kelson, D.D., van Dokkum, P.G., & Tran, K.-V. 1997, *ApJ*, 486, L75
- Giavalisco, M., & Dickinson, M. 2001, *ApJ*, 550, 177
- Giavalisco, M., Macchetto, F.D., Madau, P., & Sparks, W.B. 1995, *ApJ*, 441, L13
- Giavalisco, M., Macchetto, F.D., Sparks, W.B. 1994, *A&A*, 288, 103
- Giavalisco, M., Steidel, C.C., Adelberger, K.L., Dickinson, M.E., Pettini, M., & Kellogg, M. 1998, *ApJ*, 503, 543

- Green, R.F. 1976, *PASP*, 88, 665
- Guhathakurta, P., Tyson, J.A., & Majewski, S.R. 1990, *ApJ*, 357, 9
- Gunn, J.E., & Stryker, L.L. 1983, *ApJS*, 512, 121
- Heap, S.R., Williger, G.M., Smette, A., Hubeny, I., Sahu, M.S., Jenkins, E.B., Tripp, T.M., & Winkler, J.N. 2000, *ApJ*, 534, 69
- Koo, D.C., & Kron, R.G. 1988, *ApJ*, 333, 586
- Koo, D.C., & Kron, R.G. 1980, *PASP*, 92, 537
- Labbé, I., Franx, M., Rudnick, G., Forster-Schreiber, N.M., Van der Werf, P., Rottgering, H., van Starkenburg, L., van de Wel, A., Kuijken, K., Rix, H.-W., Moorwood, A., Daddi, E., & van Dokkum, P. 2003, *ApJ*, in press (astro-ph/0212236)
- Lilly, S.J. 1988, *ApJ*, 333, 161
- Lilly, S.J., Cowie, L.L., & Gardner, J.P. 1991, *ApJ*, 369, 79
- Lilly, S.J., Le Fèvre, O., Hammer, F., & Crampton, D. 1996, *ApJ*, 460, 1
- Lowenthal, J.D., Koo, D.C., Guzman, R., Gallego, J., Phillips, A.C., et al 1997, *ApJ*, 481, 673
- Massey, P., Strobel, K., Barnes, J.V., & Anderson, E. 1988, *ApJ*, 328, 315
- McCarthy, P.J., Carlberg, R.G., Chen, H.-W., Marzke, R.O., Firth, A.E., Ellis, R.S., Persson, S.E., et al 2001, *ApJ*, 560, L131
- McCarthy, J.K., Cohen, J.G., Butcher, B., Cromer, J., Croner, E., Douglas, W.R., Goeden, R.M., Grewal, T., Lu, B., Petrie, H.L., et al 1998, *SPIE*, 3355, 81
- Macchetto, F., Lipari, S., Giavalisco, M., Turnshek, D., & Sparks, W.B. 1993, *ApJ*, 404, 51
- Meier, D.L. 1976, *ApJ*, 207, 343
- Monet, D., et al. 1996, *USNO-SA2.0*, (U.S. Naval Observatory, Washington, D.C.)
- Nandra, K., Mushotzky, R.F., Arnaud, K., Steidel, C.C., Adelberger, K.L., Gardner, J.P., Teplitz, H.I., & Windhorst, R.A. 2002, *ApJ*, 576, 625
- Oke, J.B. 1990, *AJ*, 99, 1621
- Oke, J.B., Cohen, J.G., Carr, M., Cromer, J., Dingizian, A., Harris, F.H., Labrecque, S., Lucinio, R., Schaal, W., Epps, H., & Miller, J. 1995, *PASP*, 107, 3750
- Partridge, R.B., and Peebles, P.J.E. 1967, *ApJ*, 148, 377
- Pettini, M., Rix, S.A., Steidel, C.C., Adelberger, K.L., Hunt, M.P., & Shapley, A.E. 2002, *ApJ*, 569, 742
- Pettini, M., Shapley, A.E., Steidel, C.C., Cuby, J.-G., Dickinson, M., Moorwood, A.F.M., Adelberger, K.L., & Giavalisco, M. 2001, *ApJ*, 554, 981
- Pettini, M., Steidel, C.C., Adelberger, K.L., Dickinson, M., & Giavalisco, M. 2000, *ApJ*, 528, 96
- Pettini, M., Kellogg, M., Steidel, C.C., Dickinson, M., Adelberger, K.L., and Giavalisco, M. 1998, *ApJ*, 508, 539
- Porciani, C., and Giavalisco, M. 2002, *ApJ*, 565, 24
- Pritchett, C.J. 1994, *PASP*, 106, 1052
- Sargent, W.L.W., Steidel, C.C., & Boksenberg, A. 1989, *ApJS*, 69, 703
- Sargent, W.L.W., Boksenberg, A., & Steidel, C.C. 1988, *ApJS*, 68, 539

- Schlegel, D., Finkbeiner, D., & Davis, M. 1998, *ApJ*, 500, 525
- Shapley, A.E., Steidel, C.C., Adelberger, K.L., Dickinson, M., Giavalisco, M., & Pettini, M. 2001, *ApJ*, 562, 95
- Shapley, A.E., Steidel, C.C., Pettini, M., & Adelberger 2003, *ApJ*, in press (astro-ph/0301230)
- Songaila, A., Cowie, L.L., Hu, E.M., & Gardner, J.P. 1994, *ApJS*, 94, 461
- Steidel, C.C. 2000, *SPIE*, 4005, 22
- Steidel, C.C. 1990a, *ApJS*, 74, 37
- Steidel, C.C. 1990b, *ApJS*, 72, 1
- Steidel, C.C., Hunt, M.P., Shapley, A.E., Adelberger, K.L., Pettini, M., Dickinson, M., & Giavalisco, M. 2002, *ApJ*, 576, 653
- Steidel, C.C., Pettini, M., & Adelberger, K.L. 2001, *ApJ*, 546, 665
- Steidel, C.C., Adelberger, K.L., Shapley, A.E., Pettini, M., Dickinson, M., & Giavalisco, M. 2000, *ApJ*, 532, 170
- Steidel, C.C., Adelberger, K.L., Giavalisco, M., Dickinson, M., & Pettini, M. 1999, *ApJ*, 519, 1
- Steidel, C.C., Adelberger, K.L., Giavalisco, M., Dickinson, M., Pettini, M., & Kellogg, M. 1998, *ApJ*, 492, 428
- Steidel, C.C., Giavalisco, M., Pettini, M., Dickinson, M., & Adelberger, K.L. 1996a, *ApJL*, 462, L17
- Steidel, C.C., Giavalisco, M., Dickinson, M., & Adelberger, K.L. 1996b, *AJ*, 112, 352
- Steidel, C.C., Pettini, M., & Hamilton, D. 1995, *AJ*, 110, 2519
- Steidel, C.C., & Hamilton, D. 1992, *AJ*, 104, 941
- Steidel, C.C., & Hamilton, D. 1993, *AJ*, 105, 2017
- Tyson, J.A. 1988, *AJ*, 91, 1
- Warren, S.J., Hewett, P.C., & Osmer, P.S. 1991, *ApJS*, 76, 1
- Williams, R.E., Blacker, B., Dickinson, M., Dixon, W., Ferguson, H.C., et al 1996, *AJ*, 112, 1335
- Wolfe, A.M., Turnshek, D.A., Smith, H.E., & Cohen, R.D. 1986, *ApJS*, 61, 249

Table 1. Deep Imaging Observations

Field Name	RA(J2000) ^a	Dec(J2000) ^a	Filter	Telescope & Date ^b	Scale	FWHM	Exp Time	Dim	Area
Q0000-263	00:03:25.01	−26:03:36.8	U_n	NTT 1994 Oct	0.268	1.18	27600	3.69×5.13	18.9
			G	NTT 1994 Oct		1.04	10800		
			\mathcal{R}	NTT 1994 Oct		1.00	7200		
			I	LCO 1996 Jul		0.245	15600		
CDFa	00:53:22.97	+12:33:46.3	U_n	P200 1996 Oct	0.283	0.98	23400	8.80×8.91	78.4
			G	P200 1996 Oct		0.87	8400		
			\mathcal{R}	P200 1996 Oct		0.78	6300		
			I	P200 1997 Mar		0.89	6600		
CDFb	00:53:41.62	+12:25:10.7	U_n	P200 1997/Aug 1998 Aug	0.283	1.17	20550	9.05×9.10	82.4
			G	P200 1997 Aug/1998 Aug		1.00	6000		
			\mathcal{R}	P200 1997 Aug/1998 Aug		0.79	5400		
			I	P200 1998 Aug		1.14	7800		
Q0201+1120	02:03:46.58	+11:34:22.2	U_n	P200 1995 Nov	0.283	0.95	27000	8.69×8.72	75.7
			G	P200 1995 Nov		0.83	6300		
			\mathcal{R}	P200 1995 Nov		0.71	3600		
Q0256-000	02:59:05.13	+00:11:06.8	U_n	P200 1995 Nov/1996 Nov	0.283	1.32	35400	8.54×8.46	72.2
			G	P200 1995 Nov/1996 Nov		1.12	9600		
			\mathcal{R}	P200 1995 Nov/1996 Nov		0.91	6200		
			I	P200 1998 Sep		0.95	9800		
Q0302-003	03:04:22.65	−00:14:32.2	U_n	WHT 2000 Oct	0.236	1.15	16200	15.59×15.71	244.9
			G	WHT 2000 Oct/KPNO 2000 Dec		1.13	13800		
			\mathcal{R}	WHT 2000 Oct/KPNO 2000 Dec		0.99	13800		
			I	KPNO 2000 Dec		0.86	11400		
B20902+34	09:05:31.23	+34:08:01.7	U_n	WHT 1997 Mar	0.420	1.09	27000	6.36×6.57	41.8
			G	P200/WHT 1997 Mar		0.89	8800		
			\mathcal{R}	P200/WHT 1997 Mar		0.88	4800		
			I	P200 1997 Mar		0.90	5400		
Q0933+2854	09:33:36.09	+28:45:34.8	U_n	KPNO 2000 Dec/P200 2000 Mar	0.283	1.09	36000	8.93×9.28	82.9
			G	KPNO 2000 Dec/P200 2000 Mar		0.96	12000		
			\mathcal{R}	KPNO 2000 Dec/P200 2000 Mar		0.97	11000		
			I	KPNO 2000 Dec/P200 2000 Mar		0.90	12600		
HDF-N	12:36:51.31	+62:13:14.3	U_n	P200 1996 Mar/Apr	0.283	1.28	23400	8.62×8.73	75.3
			G	P200 1996 Mar/Apr		1.10	7200		
			\mathcal{R}	P200 1996 Mar/Apr		1.04	6000		
			I	P200 2000 Mar		1.19	5400		
Westphal	14:17:43.21	+52:28:48.5	U_n	KPNO 1996 May	0.471	1.22	25200	15.02×15.10	226.9
			G	KPNO 1996 May		1.22	7200		
			\mathcal{R}	KPNO 1996 May/P200 1997 Mar		1.18	8300		
Q1422+2309	14:24:36.98	+22:53:49.6	U_n	WHT 1999 May	0.236	0.79	30600	7.28×15.51	113.0
			G	WHT 1999 May		0.74	9600		
			\mathcal{R}	WHT 1999 May		0.67	6600		
3C 324	15:49:49.75	+21:28:48.1	U_n	WHT 1997 Mar/P200 1997 Mar	0.420	1.12	23400	6.65×6.63	44.1
			G	WHT 1997 Mar		1.09	7200		
			\mathcal{R}	WHT 1997 Mar		1.14	4800		
			I	P200 1997 Mar		0.88	3600		

Table 1—Continued

Field Name	RA(J2000) ^a	Dec(J2000) ^a	Filter	Telescope & Date ^b	Scale	FWHM	Exp Time	Dim	Area
SSA22a	22:17:33.82	+00:15:04.4	U_n	P200 1995 Aug/1996 Aug	0.283	1.03	26000	8.74×8.89	77.7
			G	P200 1995 Aug/1996 Aug		1.02	6300		
			\mathcal{R}	P200 1995 Aug/1996 Aug		1.04	6000		
			I	P200 1998 Aug		0.89	7200		
SSA22b	22:17:33.83	+00:06:21.8	U_n	P200 1996 Aug/Oct	0.283	1.08	33050	8.64×8.98	77.6
			G	P200 1996 Aug/Oct		0.90	8100		
			\mathcal{R}	P200 1996 Aug/Oct		0.90	8100		
			I	P200 1998 Aug		0.86	6600		
DSF2237a	22:40:08.32	+11:52:41.1	U_n	P200 1997 Aug/1998 Aug	0.283	0.96	23400	9.08×9.08	83.4
			G	P200 1997 Aug/1998 Aug		0.99	6900		
			\mathcal{R}	P200 1997 Aug/1998 Aug		0.94	6300		
			I	P200 1998 Aug		1.04	7200		
DSF2237b	22:39:34.10	+11:51:38.8	U_n	P200 1997 Aug	0.283	0.98	23400	8.99×9.08	81.7
			G	P200 1997 Aug		0.86	8400		
			\mathcal{R}	P200 1997 Aug		0.84	6900		
			I	P200 1998 Aug		0.81	6000		
Q2233+1341	22:36:08.76	+13:56:22.2	U_n	P200 1999 Aug/Oct	0.283	1.18	20820	9.25×9.25	85.6
			G	P200 1999 Aug/Oct		1.18	15600		
			\mathcal{R}	P200 1999 Aug/Oct		1.09	14100		
			I	P200 1999 Oct		0.95	16200		

^aPositions of the field centers.

^bP200: Palomar 5.08m telescope ; WHT: William Herschel 4.2m telescope ; LCO: Las Campanas Observatory DuPont 2.5m telescope ; NTT: ESO 3.6m New Technology Telescope; KPNO: Kitt Peak 4m Mayall telescope.

Table 2. Photometry

Field Name	E(B–V)	$\sigma(U_n)^a$	$\sigma(G)^a$	$\sigma(\mathcal{R})^a$	$\langle N \rangle^b$	$\langle G - \mathcal{R} \rangle^c$	$\langle U_n - G \rangle^c$
Q0000–263	0.000	28.80	28.64	28.06	29.3 ± 1.4	0.81 ± 0.02	0.46 ± 0.02
CDFa	0.040	28.37	28.72	28.16	25.8 ± 0.6	0.76 ± 0.01	0.51 ± 0.01
CDFb	0.040	28.23	28.47	27.93	22.9 ± 0.6	0.77 ± 0.01	0.47 ± 0.01
Q0201+113	0.142	28.16	28.47	27.86	29.2 ± 0.6	0.79 ± 0.01	0.58 ± 0.01
Q0256–000	0.085	28.41	28.34	27.96	26.7 ± 0.6	0.77 ± 0.01	0.63 ± 0.01
Q0302–003	0.089	28.02	28.66	28.14	25.2 ± 0.3	0.68 ± 0.01	0.68 ± 0.01
B20902+34	0.025	28.43	28.58	27.73	26.9 ± 0.8	0.70 ± 0.02	0.54 ± 0.02
Q0933+289	0.023	28.35	28.82	28.31	23.5 ± 0.6	0.74 ± 0.01	0.57 ± 0.01
HDF-N	0.000	27.84	28.41	27.98	25.5 ± 0.6	0.76 ± 0.01	0.53 ± 0.01
Westphal	0.000	28.32	28.11	27.33	25.0 ± 0.3	0.82 ± 0.01	0.55 ± 0.01
Q1422+2309	0.032	29.42	29.36	28.49	29.4 ± 0.4	0.80 ± 0.01	0.65 ± 0.01
3C324	0.039	28.24	28.49	27.67	23.7 ± 0.8	0.76 ± 0.02	0.59 ± 0.02
SSA22a	0.080	28.11	28.13	27.78	25.5 ± 0.6	0.74 ± 0.01	0.56 ± 0.01
SSA22b	0.080	28.16	28.53	28.26	25.1 ± 0.6	0.75 ± 0.01	0.47 ± 0.01
DSF2237a	0.048	28.36	28.54	28.08	26.2 ± 0.6	0.78 ± 0.01	0.56 ± 0.01
DSF2237b	0.048	28.53	29.00	28.47	24.6 ± 0.6	0.70 ± 0.01	0.62 ± 0.01
Q2233+1341	0.048	28.19	28.50	27.96	25.5 ± 0.6	0.85 ± 0.01	0.57 ± 0.01
Average ^d					25.9 ± 1.9	0.76 ± 0.04	0.56 ± 0.06

^aOne sigma limits for objects having an isophotal size equivalent to 3 times the seeing disk (see text).

^bMean number of detected galaxies per square arc minute in the \mathcal{R} magnitude range 22.5 – 25.0. This statistic provides an estimate of field-to-field fluctuations that should be largely independent of depth and seeing among the fields surveyed.

^cMean color of galaxies significantly detected in U_n and G to the survey limit in \mathcal{R} . This statistic provides an idea of the consistency in the galaxy colors from field to field (see text).

^dUnweighted average values from field to field, where the quoted uncertainties are the field-to-field scatter in the mean quantities.

Table 3. Typical Photometric Uncertainties and Biases

\mathcal{R} Range ^a	$G - \mathcal{R}$ Range ^b	$\Delta \mathcal{R}$ ^c	$\sigma(\mathcal{R})$ ^d	$\Delta(G - \mathcal{R})$ ^e	$\sigma(G - \mathcal{R})$ ^f
22.50–23.00	0.00–0.20	−0.03	0.09	0.02	0.04
	0.20–0.40	−0.06	0.10	0.02	0.05
	0.40–0.60	−0.08	0.12	0.03	0.06
	0.60–0.80	−0.08	0.12	0.03	0.08
	0.80–1.00	−0.08	0.12	0.05	0.08
23.00–23.50	1.00–1.20	−0.08	0.12	0.04	0.11
	0.00–0.20	−0.07	0.12	0.02	0.04
	0.20–0.40	−0.07	0.12	0.02	0.05
	0.40–0.60	−0.07	0.12	0.02	0.07
	0.60–0.80	−0.07	0.12	0.03	0.07
23.50–24.00	0.80–1.00	−0.08	0.12	0.05	0.08
	1.00–1.20	−0.08	0.12	0.05	0.12
	0.00–0.20	−0.08	0.14	0.02	0.07
	0.20–0.40	−0.08	0.14	0.01	0.07
	0.40–0.60	−0.08	0.14	0.03	0.08
24.00–24.50	0.60–0.80	−0.08	0.14	0.04	0.09
	0.80–1.00	−0.08	0.14	0.05	0.08
	1.00–1.20	−0.09	0.15	0.05	0.12
	0.00–0.20	−0.07	0.18	0.00	0.10
	0.20–0.40	−0.07	0.18	0.01	0.10
24.50–25.00	0.40–0.60	−0.07	0.18	0.03	0.11
	0.60–0.80	−0.07	0.18	0.05	0.13
	0.80–1.00	−0.07	0.18	0.08	0.15
	1.00–1.20	−0.08	0.19	0.09	0.16
	0.00–0.20	−0.02	0.21	−0.03	0.13
25.00–25.50	0.20–0.40	−0.02	0.21	0.00	0.13
	0.40–0.60	−0.02	0.21	0.03	0.13
	0.60–0.80	−0.02	0.21	0.06	0.16
	0.80–1.00	−0.02	0.21	0.10	0.17
	1.00–1.20	−0.02	0.21	0.13	0.20
	0.00–0.20	−0.02	0.23	−0.07	0.15
	0.20–0.40	−0.02	0.23	−0.03	0.16
	0.40–0.60	−0.02	0.23	0.01	0.17
	0.60–0.80	−0.02	0.23	0.07	0.19
	0.80–1.00	−0.02	0.23	0.13	0.20
	1.00–1.20	−0.02	0.25	0.16	0.24

^aRecovered magnitude range for artificial galaxies satisfying the Lyman break galaxy selection criteria.

^bRecovered color range for artificial galaxies satisfying the LBG selection criteria.

^cThe average value of $\mathcal{R}_{\text{meas}} - \mathcal{R}_{\text{true}}$. Significant departures from zero imply significant biases in the photometry.

^dThe RMS of the difference between recovered \mathcal{R} magnitudes and input magnitudes.

^eThe average value of $(G - \mathcal{R})_{\text{meas}} - (G - \mathcal{R})_{\text{true}}$ for objects recovered as LBG candidates

^fThe RMS of the difference between recovered $G - \mathcal{R}$ colors and the true input colors.

Table 4. Lyman Break Galaxy Photometric Selection Criteria

Candidate Type	Criteria
C	$\mathcal{R} \leq 25.5$; $(G - \mathcal{R}) \leq 1.2$; $(U_n - G) > (G - \mathcal{R}) + 1.5$; undetected in U_n
D	$\mathcal{R} \leq 25.5$; $(G - \mathcal{R}) \leq 1.2$; $(U_n - G) > (G - \mathcal{R}) + 1.5$; detected in U_n
M	$\mathcal{R} \leq 25.5$; $(G - \mathcal{R}) \leq 1.2$; $1.0 \leq (U_n - G) - (G - \mathcal{R}) \leq 1.5$; undetected in U_n
MD	$\mathcal{R} \leq 25.5$; $(G - \mathcal{R}) \leq 1.2$; $1.0 \leq (U_n - G) - (G - \mathcal{R}) \leq 1.5$; detected in U_n

Table 5. Spectroscopic Observations

Field Name	N(Cand) ^a	N(Obs) ^b	N($z > 2$) ^c	N(Int) ^d	f_{obs} ^e	f_{LBG} ^f	f_{int} ^g
Q0000–263	28	22	19	1	0.79	0.86	0.05
CDFa	100	60	40	1	0.60	0.67	0.02
CDFb	121	44	29	0	0.36	0.66	0.00
Q0201+113	87	32	21	0	0.37	0.66	0.00
Q0256–000	120	76	55	1	0.63	0.72	0.06
Q0302–003	191	94	50	3	0.49	0.53	0.02
B20902+34	78	46	38	2	0.59	0.83	0.05
Q0933+289	211	129	76	4	0.61	0.59	0.02
HDF-N	132	68	47	0	0.52	0.69	0.00
Westphal	329	232	188	7	0.71	0.81	0.04
Q1422+2309	273	167	120	5	0.61	0.72	0.04
($\mathcal{R} \leq 26.0$) ^h	453	195	135	5	0.43	0.69	0.04
3C324	51	12	11	0	0.24	0.92	0.00
SSA22a	146	72	57	6	0.49	0.79	0.10
SSA22b	89	48	34	1	0.54	0.71	0.03
DSF2237a	121	57	44	5	0.47	0.77	0.10
DSF2237b	176	68	58	4	0.39	0.85	0.06
Q2233+1341	94	66	53	5	0.70	0.80	0.09
TOTAL ⁱ	2347	1293	940	45	0.55	0.73	0.05

^aNumber of LBG candidates in field.

^bNumber of LBG candidates observed spectroscopically.

^cNumber of spectroscopically identified LBG candidates with $z > 2$.

^dNumber of spectroscopically identified “interlopers”. Of the total of 45, 40 are stars, 2 are galaxies with $z \simeq 1.98$, and 3 are absorption line galaxies at $z \sim 0.5$ (see text).

^eThe fraction of LBG candidates observed spectroscopically.

^fThe fraction of spectroscopically observed candidates with measured $z > 2$.

^gThe fraction of “interlopers” among spectroscopically identified LBG candidates.

^hFor objects with $\mathcal{R} \leq 26.0$; all other catalogs are limited at $\mathcal{R} \leq 25.5$.

ⁱThe total numbers include only candidates with $\mathcal{R} \leq 25.5$, and so the numbers do not include the 28 objects (15 of which yielded successful redshifts) fainter than $\mathcal{R} = 25.5$ observed in the Q1422+2309 field.

Table 6. Redshift Statistics for LBG Candidates with $\mathcal{R} \leq 25.5$

Candidate Type	N(Cand) ^a	N(obs) ^b	N($z > 2$) ^c	f_{obs} ^d	f_{LBG} ^e	f_{Int} ^f	$\langle z \rangle$ ^g
C	526	366	291	0.70	0.80	0.03	3.09 ± 0.22
D	343	237	197	0.69	0.83	0.02	2.93 ± 0.26
M	449	197	136	0.44	0.69	0.02	3.15 ± 0.24
MD	1029	486	316	0.47	0.65	0.08	2.79 ± 0.27
Total	2347	1286	940	0.55	0.73	0.05	2.96 ± 0.29
S99 ^h	1892	1104	822	0.58	0.74	0.05	3.01 ± 0.27

^aNumber of photometric candidates.

^bNumber of objects spectroscopically observed.

^cNumber of objects with confirmed redshifts $z > 2$.

^dThe fraction of candidates observed spectroscopically.

^eThe fraction of spectroscopically observed candidates yielding confirmed redshifts $z > 2$.

^fThe fraction of spectroscopically identified objects that have $z < 2$.

^gMean and standard deviation of the redshift distribution for objects with $z > 2$.

^hNumber of objects satisfying the photometric criteria used in Steidel et al. 1999. These criteria exclude objects with $U_n - G < 1.6$.

Table 7. Q0000–263 Field LBGs

Name	$\alpha(J2000)$	$\delta(J2000)$	\mathcal{R}	$G - \mathcal{R}$	$U_n - G$	z_{em}	z_{abs}	Type	Notes ^a
Q0000-C1	00:03:17.13	-26:06:03.2	25.38	0.60	2.86	-1.000	-1.000	—	
Q0000-C2	00:03:30.38	-26:05:47.3	25.23	0.65	3.07	-1.000	-1.000	—	
Q0000-C3	00:03:27.58	-26:05:45.0	23.99	1.17	3.50	0.000	0.000	STAR	S96-C02
Q0000-C4	00:03:21.87	-26:05:39.9	24.57	1.06	2.87	3.594	3.580	GAL	
Q0000-C5	00:03:28.94	-26:05:26.1	23.62	1.08	4.12	3.791	-2.000	QSO	S96-C04
Q0000-C6	00:03:21.12	-26:04:17.4	25.22	1.00	2.73	-2.000	3.389	GAL	S96-C07
Q0000-C7	00:03:28.85	-26:03:53.3	24.21	0.07	4.40	3.426	-2.000	AGN	S96-C09; G2 ^b
Q0000-C8	00:03:20.25	-26:03:36.6	24.47	0.89	3.32	-2.000	3.427	GAL	S96-C10
Q0000-C9	00:03:26.33	-26:03:28.7	25.03	1.02	2.78	-1.000	-1.000	—	
Q0000-C10	00:03:23.30	-26:02:52.3	24.78	0.84	3.08	-2.000	2.960	GAL	S96-C13
Q0000-C12	00:03:27.31	-26:02:27.7	24.37	0.63	3.56	3.021	-2.000	GAL	S96-C14
Q0000-C13	00:03:25.40	-26:01:25.3	25.03	0.76	2.84	-2.000	-2.000	—	
Q0000-C14	00:03:30.39	-26:01:20.7	24.47	0.86	3.24	3.057	3.053	AGN	S96-C16
Q0000-D1	00:03:25.17	-26:04:35.2	24.32	0.49	2.20	2.788	-2.000	GAL	S96-C22
Q0000-D2	00:03:31.02	-26:04:31.1	25.23	0.34	2.45	-1.000	-1.000	—	
Q0000-D3	00:03:17.23	-26:04:03.9	24.91	0.51	3.33	3.143	3.147	GAL	S96-C08
Q0000-D4	00:03:20.97	-26:03:37.6	24.79	0.47	2.09	-2.000	2.775	GAL	S96-C27
Q0000-D5	00:03:28.51	-26:03:28.3	24.96	0.54	2.23	3.150	3.139	GAL	S96-C11
Q0000-D6	00:03:23.79	-26:02:48.5	22.88	0.45	2.26	2.971	2.958	GAL	
Q0000-D8	00:03:32.45	-26:01:47.4	24.76	0.62	2.64	-2.000	3.041	GAL	S96-C25
Q0000-M1	00:03:19.84	-26:01:22.1	25.05	1.03	2.42	-2.000	3.168	GAL	S96-C17
Q0000-MD1	00:03:24.65	-26:05:48.8	25.38	0.72	2.25	3.602	3.589	GAL	
Q0000-MD2	00:03:25.12	-26:04:52.6	24.88	1.11	2.28	3.596	-2.000	GAL	S96-C05
Q0000-MD3	00:03:18.47	-26:04:35.0	23.75	0.54	1.76	-2.000	3.201	GAL	S96-C23
Q0000-MD4	00:03:19.70	-26:04:26.5	24.82	0.49	1.70	-1.000	-1.000	—	
Q0000-MD5	00:03:25.92	-26:02:20.0	25.28	0.40	1.92	-2.000	-2.000	—	
Q0000-MD6	00:03:21.22	-26:01:47.6	25.41	0.66	2.03	3.092	-2.000	GAL	
Q0000-MD7	00:03:21.25	-26:01:26.8	22.68	0.74	1.76	-1.000	-1.000	—	

^a“S96-XXX” indicates object names appearing in Steidel et al. 1996a

^bThis object is discussed in Macchetto et al. 1993 and Gialalisco et al. 1994,1995

Table 8. CDFa Field LBGs*

Name	$\alpha(J2000)$	$\delta(J2000)$	\mathcal{R}	$G - \mathcal{R}$	$U_n - G$	z_{em}	z_{abs}	Type	Notes ^a
CDFa-C1	00:53:34.73	12:30:30.6	23.53	0.69	3.24	-2.000	3.113	GAL	
CDFa-C2	00:53:06.89	12:30:46.1	25.45	0.36	2.24	-1.000	-1.000	—	
CDFa-C3	00:53:14.01	12:29:46.6	24.69	0.52	2.85	-2.000	-2.000	—	
CDFa-C4	00:53:18.63	12:31:08.5	25.18	0.66	2.18	-2.000	2.628	GAL	
CDFa-C5	00:53:36.02	12:31:42.6	24.61	0.87	2.37	-2.000	-2.000	—	
CDFa-C6	00:53:39.85	12:31:45.9	25.43	0.59	2.13	2.971	2.953	GAL	
CDFa-C7	00:53:37.62	12:31:58.2	23.13	0.73	3.74	-2.000	3.072	GAL	
...

*The complete version of this table will be available in the electronic version of the paper.

Table 9. CDFb Field LBGs*

Name	$\alpha(J2000)$	$\delta(J2000)$	\mathcal{R}	$G - \mathcal{R}$	$U_n - G$	z_{em}	z_{abs}	Type	Notes ^a
CDFb-C1	00:53:38.95	12:20:54.9	25.37	0.55	2.09	-1.000	-1.000	—	
CDFb-C2	00:54:00.01	12:21:36.3	25.02	0.60	2.18	-1.000	-1.000	—	
CDFb-C3	00:53:35.71	12:21:30.7	24.18	0.84	2.73	-2.000	3.477	GAL	
CDFb-C4	00:53:48.66	12:22:08.1	25.05	0.45	2.34	-2.000	-2.000	—	
CDFb-C5	00:53:33.71	12:22:09.2	25.46	0.51	2.23	-2.000	-2.000	—	
CDFb-C6	00:53:54.46	12:22:23.3	24.59	0.69	2.41	-1.000	-1.000	—	
CDFb-C7	00:53:50.81	12:22:22.2	24.61	0.76	2.26	-1.000	-1.000	—	
...

*The complete version of this table will be available in the electronic version of the paper.

Table 10. Q0201+1120 Field LBGs*

Name	$\alpha(J2000)$	$\delta(J2000)$	\mathcal{R}	$G - \mathcal{R}$	$U_n - G$	z_{em}	z_{abs}	Type	Notes ^a
Q0201-C1	02:03:59.94	11:30:20.4	24.54	0.43	2.56	-1.000	-1.000	—	
Q0201-C2	02:03:32.97	11:31:24.2	24.22	0.95	2.75	-1.000	-1.000	—	
Q0201-C3	02:03:56.25	11:30:54.9	24.94	0.51	2.42	3.020	-2.000	GAL	
Q0201-C4	02:03:30.91	11:31:53.0	24.25	0.61	2.40	-1.000	-1.000	—	
Q0201-C5	02:03:54.34	11:31:31.2	25.46	0.32	2.29	-1.000	-1.000	—	
Q0201-C6	02:03:32.52	11:34:15.1	25.04	0.55	2.40	-1.000	-1.000	—	
Q0201-C7	02:03:36.87	11:35:31.7	24.37	0.69	2.88	3.138	3.129	GAL	
...

*The complete version of this table will be available in the electronic version of the paper.

^aObjects discussed in Ellison et al. 2001.

^bThis galaxy was previously known as Q0201-C6 in Pettini et al. 1998,2001 and in Shapley et al. 2001.

Table 11. Q0256–000 Field LBGs*

Name	$\alpha(J2000)$	$\delta(J2000)$	\mathcal{R}	$G - \mathcal{R}$	$U_n - G$	z_{em}	z_{abs}	Type	Notes ^a
Q0256-C8	02:58:57.85	00:07:58.0	24.91	0.32	2.98	-2.000	-2.000	—	
Q0256-C9	02:58:56.97	00:08:50.8	24.13	0.74	2.86	-2.000	-2.000	—	
Q0256-C10	02:58:52.51	00:09:05.6	25.07	0.63	2.25	-1.000	-1.000	—	
Q0256-C11	02:59:19.50	00:09:15.4	25.15	0.50	2.65	3.009	3.001	GAL	
Q0256-C14	02:58:53.07	00:09:53.6	24.71	0.48	2.91	:2.983	-2.000	GAL	
Q0256-C15	02:58:53.18	00:10:40.0	25.14	0.67	2.20	-2.000	2.964	GAL	
Q0256-C16	02:58:53.11	00:10:43.4	24.22	0.98	2.83	-2.000	2.974	GAL	
...

*The complete version of this table will be available in the electronic version of the paper.

^aObjects observed in the near-IR are indicated with their old designations as in Shapley et al. 2001 (for cross-referencing).

Table 12. Q0302–003 Field LBGs*

Name	$\alpha(J2000)$	$\delta(J2000)$	\mathcal{R}	$G - \mathcal{R}$	$U_n - G$	z_{em}	z_{abs}	Type	Notes
Q0302-C131	03:04:35.04	-00:11:18.3	24.48	0.54	2.57	3.240	3.227	GAL	
Q0302-C133	03:04:33.17	-00:11:46.9	24.55	0.84	2.37	-1.000	-1.000	—	
Q0302-C134	03:04:29.20	-00:11:00.3	25.18	0.37	2.41	-1.000	-1.000	—	
Q0302-C140	03:04:52.11	-00:10:21.7	25.28	0.48	2.16	-1.000	-1.000	—	
Q0302-C141	03:04:53.42	-00:10:17.1	24.33	0.56	2.48	-2.000	-2.000	—	
Q0302-C146	03:04:26.45	-00:10:06.9	25.21	0.50	2.48	-1.000	-1.000	—	
Q0302-C148	03:04:33.59	-00:09:51.2	24.27	0.51	2.67	:2.848	-2.000	GAL	
...

*The complete version of this table will be available in the electronic version of the paper.

Table 13. B20902+34 Field LBGs*

Name	$\alpha(J2000)$	$\delta(J2000)$	\mathcal{R}	$G - \mathcal{R}$	$U_n - G$	z_{em}	z_{abs}	Type	Notes ^a
B20902-C1	09:05:25.05	34:04:54.4	24.41	0.92	2.76	-1.000	-1.000	—	
B20902-C2	09:05:37.86	34:05:57.9	25.16	0.56	2.48	-2.000	2.732	GAL	
B20902-C4	09:05:45.78	34:08:18.0	24.52	0.63	2.70	3.034	3.025	GAL	
B20902-C5	09:05:23.09	34:08:59.3	24.70	0.93	2.47	-2.000	3.098	GAL	
B20902-C6	09:05:20.58	34:09:07.7	24.13	0.45	3.45	3.099	-2.000	GAL	
B20902-C7	09:05:30.11	34:09:07.7	24.52	0.37	3.16	3.195	-2.000	GAL	
...

*The complete version of this table will be available in the electronic version of the paper.

Table 14. Q0933+289 Field LBGs*

Name	$\alpha(J2000)$	$\delta(J2000)$	\mathcal{R}	$G - \mathcal{R}$	$U_n - G$	z_{em}	z_{abs}	Type	Notes ^a
Q0933-C1	09:33:20.22	28:41:16.4	25.02	0.77	2.32	-1.000	-1.000	—	
Q0933-C2	09:33:37.09	28:41:15.6	24.87	1.03	2.64	-1.000	-1.000	—	
Q0933-C3	09:33:19.53	28:41:34.1	25.42	0.38	2.14	-1.000	-1.000	—	
Q0933-C4	09:33:35.18	28:41:38.1	24.79	0.77	2.43	-1.000	-1.000	—	
Q0933-C5	09:33:47.89	28:41:41.4	24.44	0.46	2.80	-1.000	-1.000	—	
Q0933-C6	09:33:35.47	28:41:42.0	25.09	0.55	2.38	-1.000	-1.000	—	
Q0933-C7	09:33:28.64	28:41:49.5	24.99	0.70	2.41	:3.383	:3.376	GAL	
...

*The complete version of this table will be available in the electronic version of the paper.

Table 15. HDF-N Field LBGs*

Name	$\alpha(J2000)$	$\delta(J2000)$	\mathcal{R}	$G - \mathcal{R}$	$U_n - G$	z_{em}	z_{abs}	Type	Notes
HDF-C2	12:36:57.36	62:09:00.4	24.14	0.85	2.46	-1.000	-1.000	—	
HDF-C3	12:36:29.13	62:09:03.6	23.50	1.02	2.52	-2.000	-2.000	—	
HDF-C4	12:37:03.34	62:09:20.4	25.16	0.41	2.02	-1.000	-1.000	—	
HDF-C5	12:36:23.87	62:09:42.7	24.88	0.42	2.23	-2.000	:2.664	GAL	
HDF-C6	12:37:16.96	62:10:02.3	24.34	0.55	2.74	3.451	-2.000	GAL	
HDF-C7	12:36:37.66	62:10:47.8	24.57	0.62	2.46	-2.000	2.658	GAL	
HDF-C8	12:36:26.95	62:11:27.4	24.38	0.70	2.35	2.993	2.983	GAL	
HDF-C9	12:37:11.12	62:11:51.9	25.26	0.35	2.04	-1.000	-1.000	—	
HDF-C10	12:36:55.77	62:12:01.1	24.36	0.53	2.35	-1.000	-1.000	—	
HDF-C11	12:36:41.26	62:12:03.4	24.41	0.86	2.50	3.222	3.214	GAL	C4-09:4-858.0 ^b
...

*The complete version of this table will be available in the electronic version of the paper.

^aObject within central HDF region observed with HST; designation as published in Steidel et al. 1996b.

^bObject within central HDF WFPC-2 region; designation as published in Williams et al. 1996.

^cRedshift from Lowenthal et al. 1997.

Table 16. Westphal Field LBGs*

Name ^a	$\alpha(J2000)$	$\delta(J2000)$	\mathcal{R}	$G - \mathcal{R}$	$U_n - G$	z_{em}	z_{abs}	Type	Notes ^a
Westphal-C1	14:18:21.97	52:21:21.9	23.83	1.02	2.93	2.992	2.986	GAL	CC1
Westphal-C2	14:17:42.22	52:21:38.5	24.70	0.83	2.56	3.143	3.131	GAL	
Westphal-C3	14:17:37.88	52:21:57.3	25.21	0.54	2.32	2.896	2.888	GAL	
Westphal-C4	14:17:28.56	52:22:03.6	24.56	0.81	2.45	-2.000	:2.967	GAL	
Westphal-C5	14:18:24.15	52:22:23.4	24.81	0.67	2.50	2.815	-2.000	GAL	
Westphal-C6	14:18:12.01	52:22:39.8	24.61	0.63	2.65	2.829	2.845	GAL	
Westphal-C7	14:18:01.21	52:22:53.9	25.27	0.71	2.23	-2.000	-2.000	—	
...

*The complete version of this table will be available in the electronic version of the paper.

^aFor purely historical reasons, a number of objects in this field have been published under slightly different names. For such cases, the previous designation is given in the “Notes” column.

Table 17. 3C 324 Field LBGs*

Name	$\alpha(J2000)$	$\delta(J2000)$	\mathcal{R}	$G - \mathcal{R}$	$U_n - G$	z_{em}	z_{abs}	Type	Notes
3C324-C1	15:49:54.27	21:26:33.1	24.33	0.62	2.52	2.890	2.878	GAL	
3C324-C2	15:49:53.98	21:26:35.5	24.26	0.54	3.00	-2.000	2.877	GAL	
3C324-C3	15:49:47.10	21:27:05.4	24.14	0.85	2.61	3.295	3.282	GAL	
3C324-C4	15:49:46.04	21:27:46.2	24.59	0.52	2.54	-2.000	3.281	GAL	
3C324-C5	15:49:44.21	21:28:22.0	24.68	0.70	2.28	-1.000	-1.000	—	
3C324-C6	15:49:38.74	21:29:17.5	24.73	0.83	2.33	3.313	3.303	GAL	
3C324-C7	15:49:47.47	21:29:21.1	25.09	0.61	2.42	-1.000	-1.000	—	
...

*The complete version of this table will be available in the electronic version of the paper.

Table 18. Q1422+2309 Field LBGs*

Name	$\alpha(J2000)$	$\delta(J2000)$	\mathcal{R}	$G - \mathcal{R}$	$U_n - G$	z_{em}	z_{abs}	Type	Notes
Q1422-C1	14:24:41.60	22:46:21.1	25.21	0.97	2.87	-1.000	-1.000	—	
Q1422-C2	14:24:31.42	22:46:41.2	25.76	0.61	2.99	-1.000	-1.000	—	
Q1422-C3	14:24:45.89	22:47:25.7	25.68	0.50	2.97	-1.000	-1.000	—	
Q1422-C4	14:24:26.54	22:47:32.0	25.69	0.81	2.38	-1.000	-1.000	—	
Q1422-C5	14:24:44.21	22:47:32.0	25.54	0.84	2.63	-1.000	-1.000	—	
Q1422-C6	14:24:22.37	22:47:40.0	24.45	0.94	3.66	-1.000	-1.000	—	
Q1422-C7	14:24:29.41	22:47:59.7	25.66	0.80	2.69	-1.000	-1.000	—	
...

*The complete version of this table will be available in the electronic version of the paper.

^aThis object does not satisfy the LBG color selection criteria, but is of interest because it is near Q1422+2309 on the plan of the sky and is at close to the same redshift.

Table 19. SSA22a Field LBGs*

Name ^a	$\alpha(J2000)$	$\delta(J2000)$	\mathcal{R}	$G - \mathcal{R}$	$U_n - G$	z_{em}	z_{abs}	Type	Notes
SSA22a-C1	22:17:31.36	00:10:41.7	25.34	0.55	2.17	-1.000	-1.000	—	
SSA22a-C2	22:17:44.52	00:10:57.6	25.31	0.46	2.07	-1.000	-1.000	—	
SSA22a-C3	22:17:32.53	00:10:57.4	25.05	0.35	2.36	-1.000	-1.000	—	
SSA22a-C4	22:17:38.89	00:11:02.1	24.53	0.42	2.54	3.076	-2.000	GAL	S98-C3
SSA22a-C6	22:17:40.93	00:11:26.0	23.44	0.79	2.97	3.098	3.092	GAL	S98-C5
SSA22a-C7	22:17:24.59	00:11:31.3	24.13	1.06	2.70	-1.000	-1.000	—	
SSA22a-C8	22:17:27.64	00:11:59.0	25.38	0.20	2.22	-1.000	-1.000	—	
...

*The complete version of this table will be available in the electronic version of the paper.

^aObjects whose photometry satisfies our LBG selection criteria, but which have been discussed under alternative names, are indicated in the “Notes” column. “S96” refers to Steidel et al. 1996a, and “S98” refers to Steidel et al. 1998. Objects which at one time satisfied our selection criteria, and which were spectroscopically observed, are included at the end of the table (see appendix).

Table 20. SSA22b Field LBGs*

Name	$\alpha(J2000)$	$\delta(J2000)$	\mathcal{R}	$G - \mathcal{R}$	$U_n - G$	z_{em}	z_{abs}	Type	Notes
SSA22b-C1	22:17:46.08	00:02:12.5	24.62	0.79	2.81	-1.000	-1.000	—	
SSA22b-C3	22:17:29.22	00:02:48.8	24.55	0.68	2.68	2.917	2.911	GAL	
SSA22b-C4	22:17:46.85	00:03:29.2	25.47	0.32	2.07	-2.000	-2.000	—	
SSA22b-C5	22:17:47.06	00:04:25.7	25.16	0.71	2.48	3.117	3.110	GAL	
SSA22b-C6	22:17:33.88	00:05:15.5	25.35	0.41	2.21	3.313	-2.000	GAL	
SSA22b-C9	22:17:22.42	00:06:47.6	24.69	0.72	2.30	3.175	3.170	GAL	
SSA22b-C10	22:17:25.46	00:06:59.2	24.11	0.93	2.62	3.360	3.353	GAL	
...

*The complete version of this table will be available in the electronic version of the paper.

^aThis object appeared as a member of the $z = 3.09$ “spike” in Steidel et al. 1998, called “SSA22b-D27”.

Table 21. DSF2237a Field LBGs*

Name	$\alpha(J2000)$	$\delta(J2000)$	\mathcal{R}	$G - \mathcal{R}$	$U_n - G$	z_{em}	z_{abs}	Type	Notes
DSF2237a-C1	22:40:15.74	11:48:14.8	24.80	0.29	2.83	-1.000	-1.000	—	
DSF2237a-C2	22:40:08.29	11:49:04.8	23.55	1.13	3.20	3.331	3.318	GAL	
DSF2237a-C3	22:40:23.15	11:49:28.6	24.48	0.75	2.64	3.111	3.107	GAL	
DSF2237a-C4	22:40:06.48	11:49:29.9	24.58	0.69	2.75	3.487	3.474	GAL	
DSF2237a-C5	22:40:22.88	11:49:38.7	25.02	0.60	2.28	-1.000	-1.000	—	
DSF2237a-C6	22:40:08.26	11:49:45.6	24.26	1.04	2.97	-2.000	3.145	GAL	
DSF2237a-C7	22:40:20.90	11:50:21.8	25.16	0.50	2.46	3.202	3.195	GAL	
...

*The complete version of this table will be available in the electronic version of the paper.

Table 22. DSF2237b Field LBGs*

Name	$\alpha(J2000)$	$\delta(J2000)$	\mathcal{R}	$G - \mathcal{R}$	$U_n - G$	z_{em}	z_{abs}	Type	Notes
DSF2237b-C1	22:39:16.90	11:47:47.5	24.99	0.37	2.53	3.068	3.057	GAL	
DSF2237b-C2	22:39:31.96	11:47:58.8	24.95	0.85	2.40	-2.000	3.142	GAL	
DSF2237b-C3	22:39:35.83	11:48:09.5	25.19	0.73	2.24	-2.000	-2.000	—	
DSF2237b-C7	22:39:32.96	11:48:17.5	25.10	0.28	2.58	-2.000	3.293	GAL	
DSF2237b-C8	22:39:36.05	11:48:17.1	24.93	0.73	2.27	3.107	3.110	GAL	
DSF2237b-C9	22:39:44.46	11:48:25.6	25.45	0.42	2.35	3.245	3.234	GAL	
DSF2237b-C10	22:39:24.33	11:48:28.5	25.10	0.60	2.55	-1.000	-1.000	—	
...

*The complete version of this table will be available in the electronic version of the paper.

Table 23. Q2233+1341 Field LBGs*

Name	$\alpha(J2000)$	$\delta(J2000)$	\mathcal{R}	$G - \mathcal{R}$	$U_n - G$	z_{em}	z_{abs}	Type	Notes
Q2233-C1	22:36:28.12	13:51:46.4	25.35	0.55	2.22	-1.000	-1.000	—	
Q2233-C2	22:36:21.64	13:52:16.3	24.20	0.90	2.49	2.970	2.964	GAL	
Q2233-C3	22:36:22.97	13:52:33.9	24.61	0.66	2.48	2.546	2.542	GAL	
Q2233-C4	22:36:16.67	13:53:58.4	24.47	1.01	2.84	3.053	-2.000	GAL	
Q2233-C5	22:36:44.87	13:54:30.7	25.32	0.42	2.08	-1.000	-1.000	—	
Q2233-C6	22:36:22.55	13:54:29.7	24.72	0.59	2.09	2.546	2.542	GAL	
Q2233-C7	22:36:12.56	13:55:14.0	24.97	1.01	2.74	-1.000	-1.000	—	
...

*The complete version of this table will be available in the electronic version of the paper.

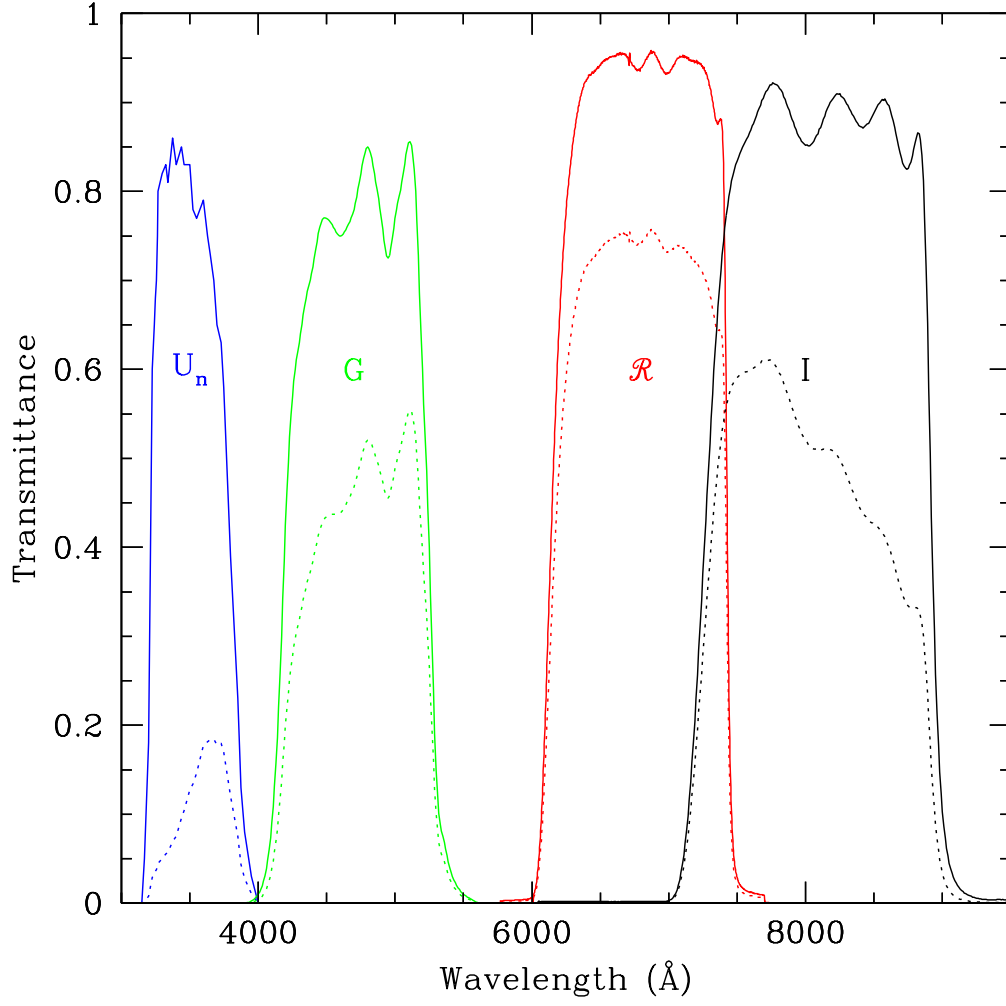


Fig. 1.— The filter system used for the deep imaging, U_n [3550/600], G [4780/1100], R [6830/1250], and I [8100/1650]. The dotted curves show the effective bandpasses including typical CCD quantum efficiency and atmospheric attenuation.

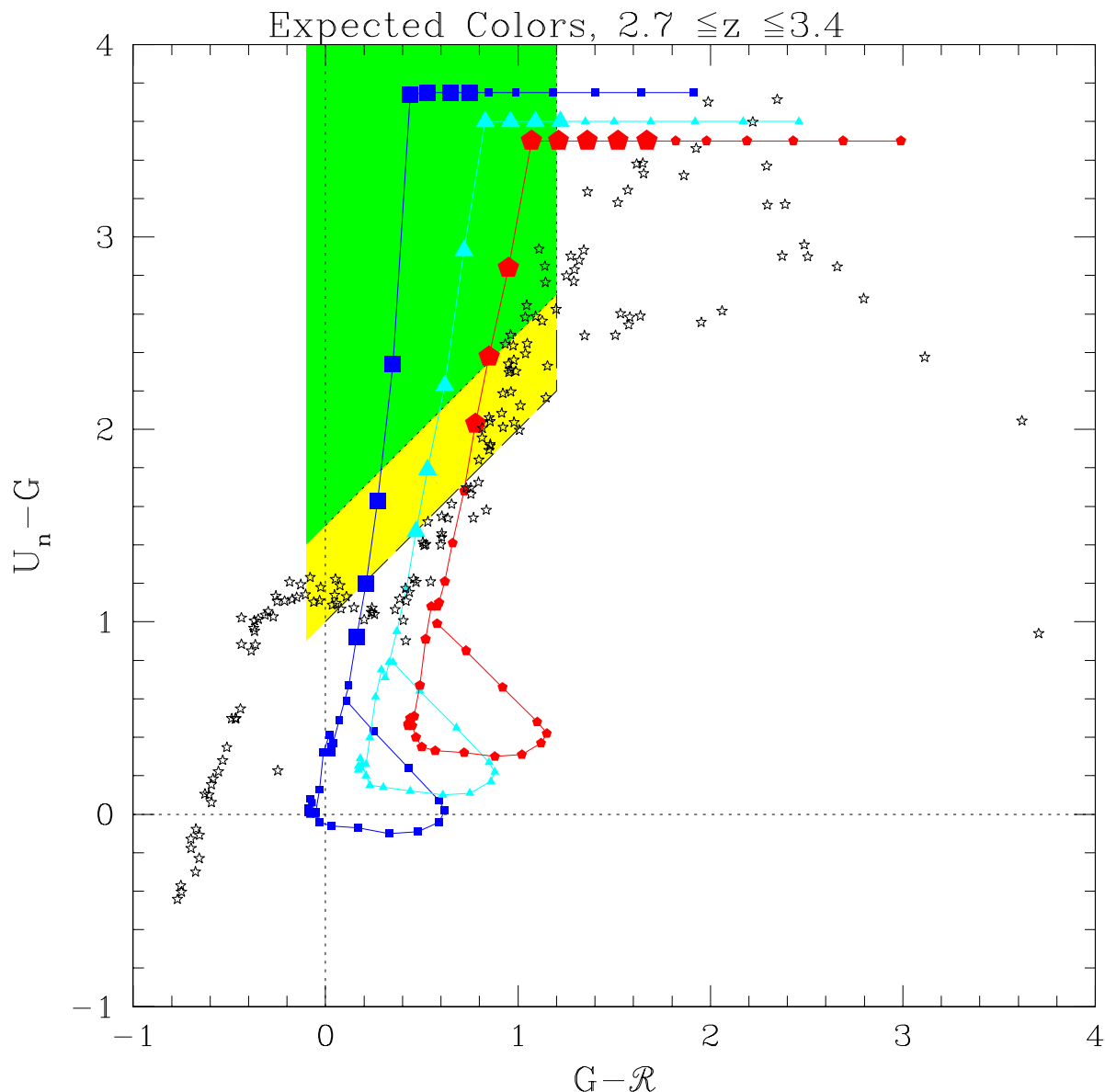


Fig. 2.— Plot showing the expected colors for model star forming galaxies in the targeted redshift range, for 3 assumed values of internal extinction ($E(B - V) = 0, 0.15, 0.30$ using the Calzetti et al. 2000 prescription, for squares, triangles, and pentagons, respectively), with points corresponding to intervals of $\Delta z = 0.1$. The large points on each curve correspond to galaxies in the redshift interval $2.7 \leq z \leq 3.4$. The $U_n - G$ colors have been truncated for clarity; in practice, limited dynamic range will prevent $U_n - G$ limits from exceeding ~ 4.0 . The green shaded region is where “C” and “D” type candidates are located; the yellow shaded region corresponds to candidate types “M” and “MD” (see Table 4). Note that the redshift distributions of LBG samples are expected to depend upon the intrinsic spectral shape of the galaxies, which we have parameterized by $E(B-V)$; conversely, the range of intrinsic colors sampled by the selection criteria will depend upon redshift. These points are discussed in some detail in Steidel et al. 1999. The expected location of the stellar locus, based on the Gunn & Stryker (1983) atlas, is shown with the black “stars”.

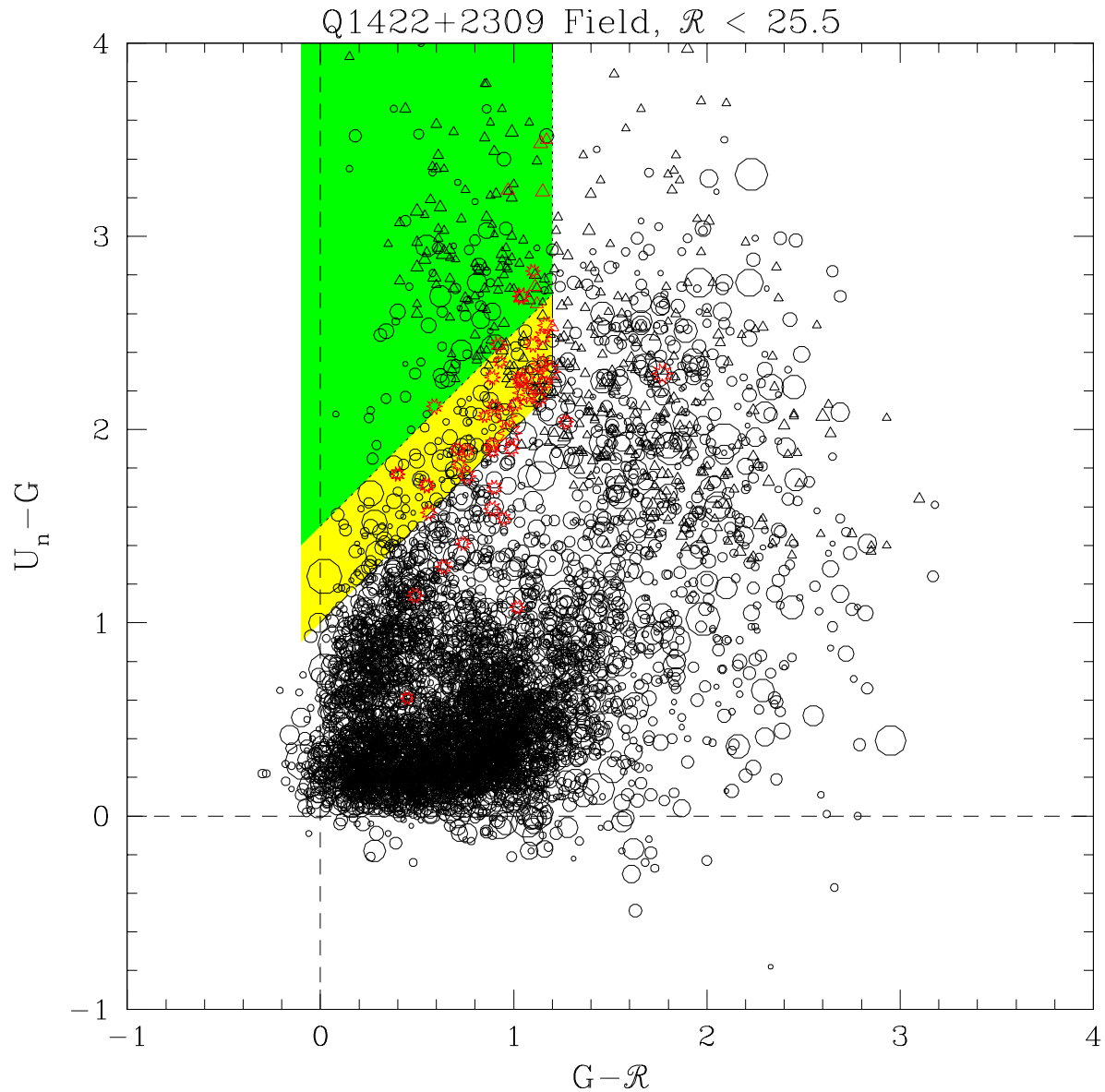


Fig. 3.— Plot showing real data, for $\mathcal{R} \leq 25.5$ objects in the Q1422+2309 field. Objects that are detected in U_n are shown with open circles (scaled according to brightness); objects having only limits on $U_n - G$ colors are shown with triangles. The locations in the two-color plane of all 55 stars (taken from all 17 of the observed fields) that have been observed spectroscopically (40 of which satisfy the LBG color criteria) are shown in red.

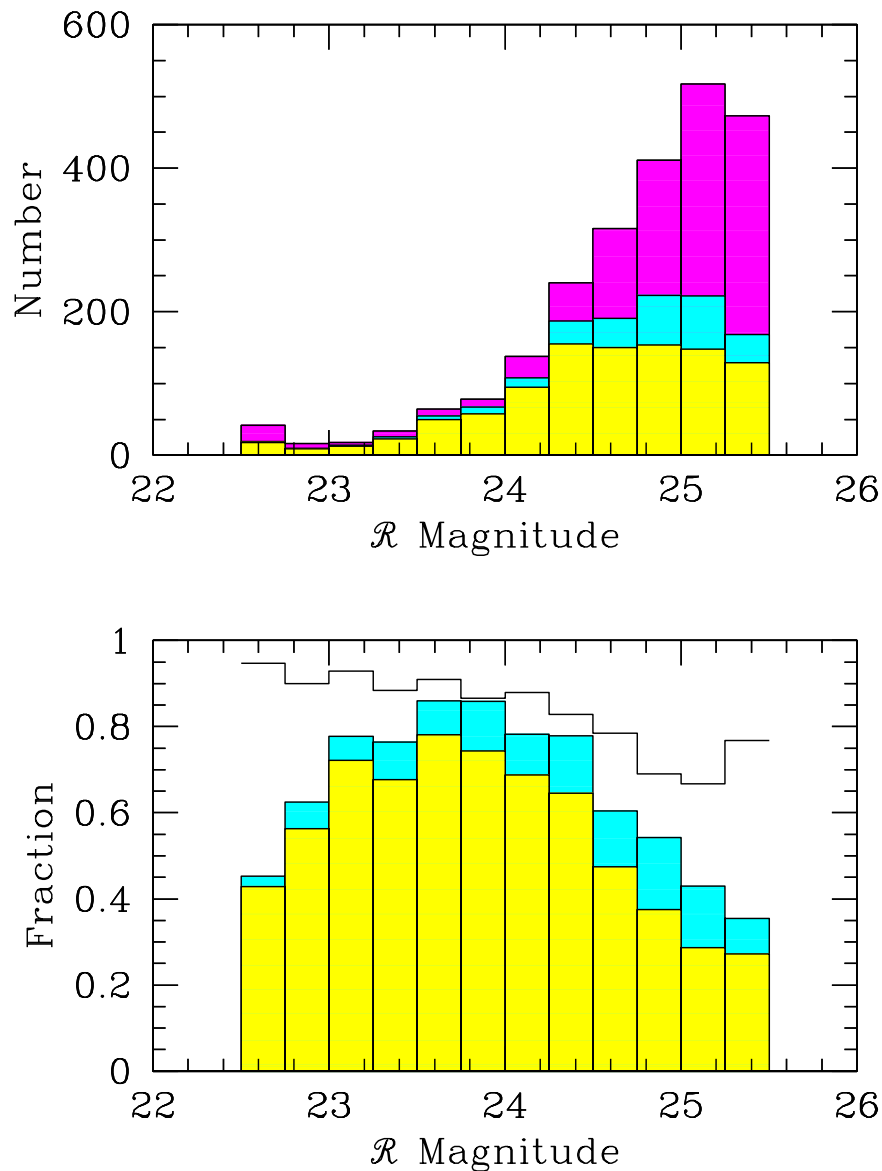


Fig. 4.— Plot showing the magnitude distribution of the full photometric LBG sample (magenta), the subsample targeted for spectroscopy (cyan), and the subsample with successful spectroscopic redshifts (yellow). The bottom panel shows the fraction of the full photometric sample represented by the spectroscopically observed subsample (cyan) and the spectroscopically successful samples versus apparent magnitude. The black curve represents the fraction of spectroscopically observed objects that yielded successful redshifts, as a function of apparent \mathcal{R} magnitude.

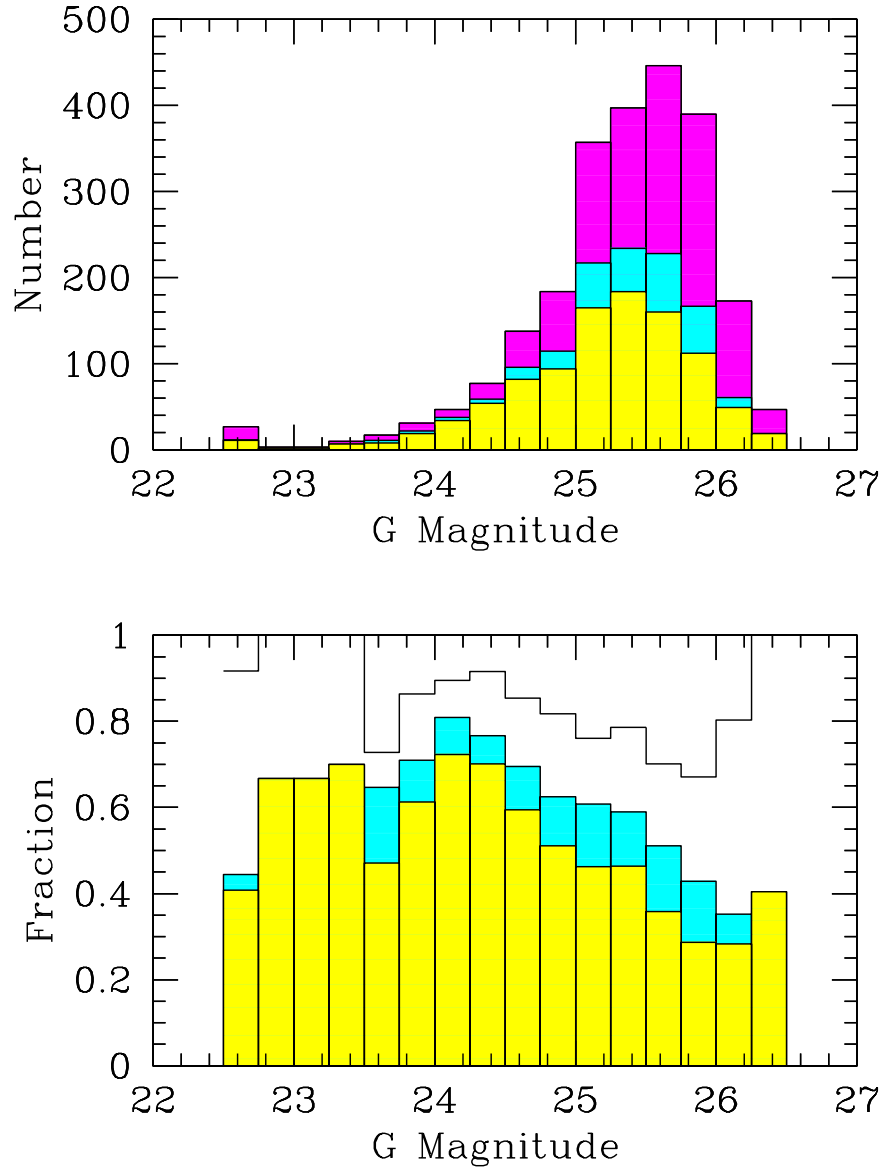


Fig. 5.— Same as Figure 4, as a function of G magnitude.

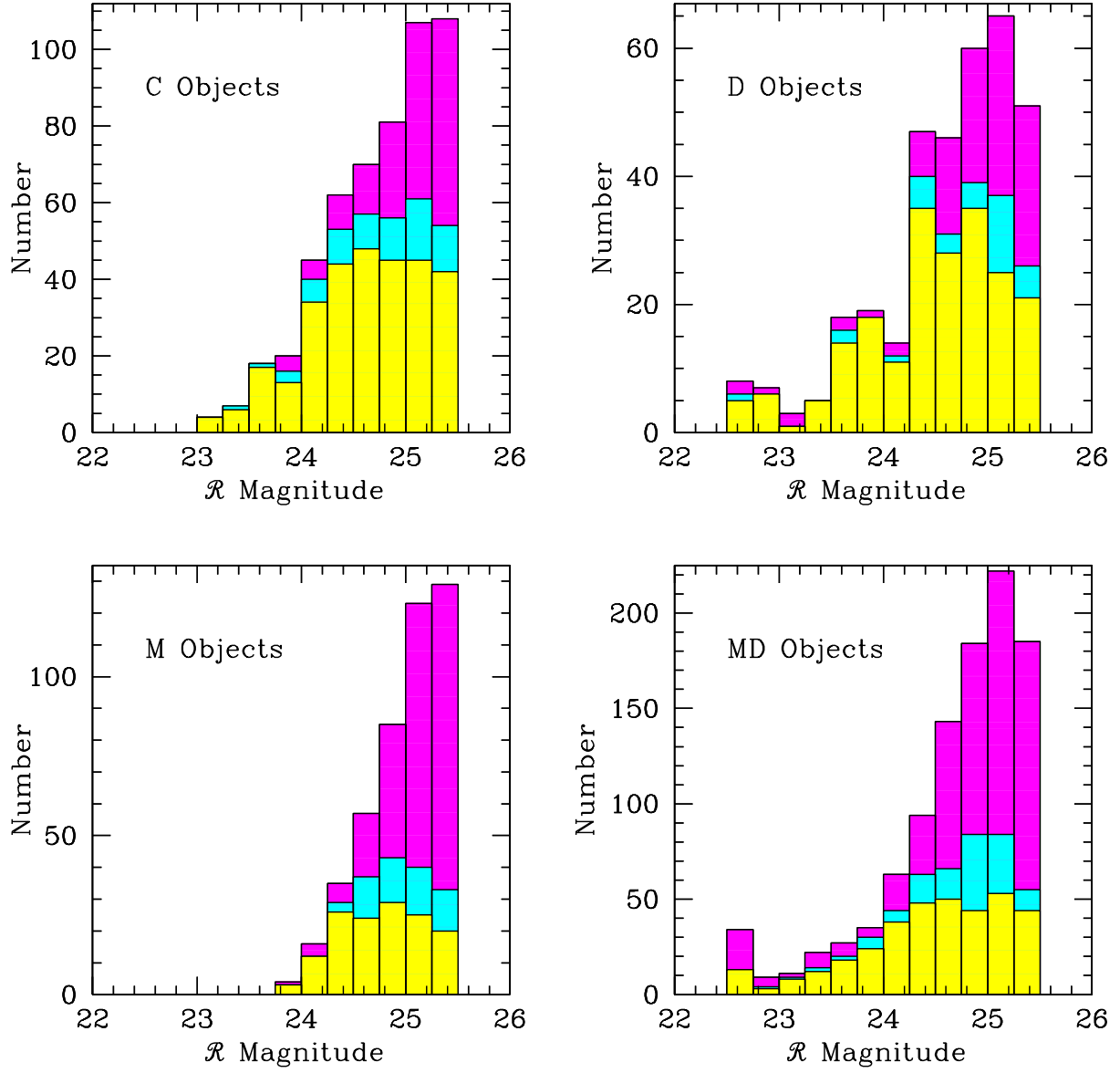


Fig. 6.— Same as figure 4, divided by candidate classification system.

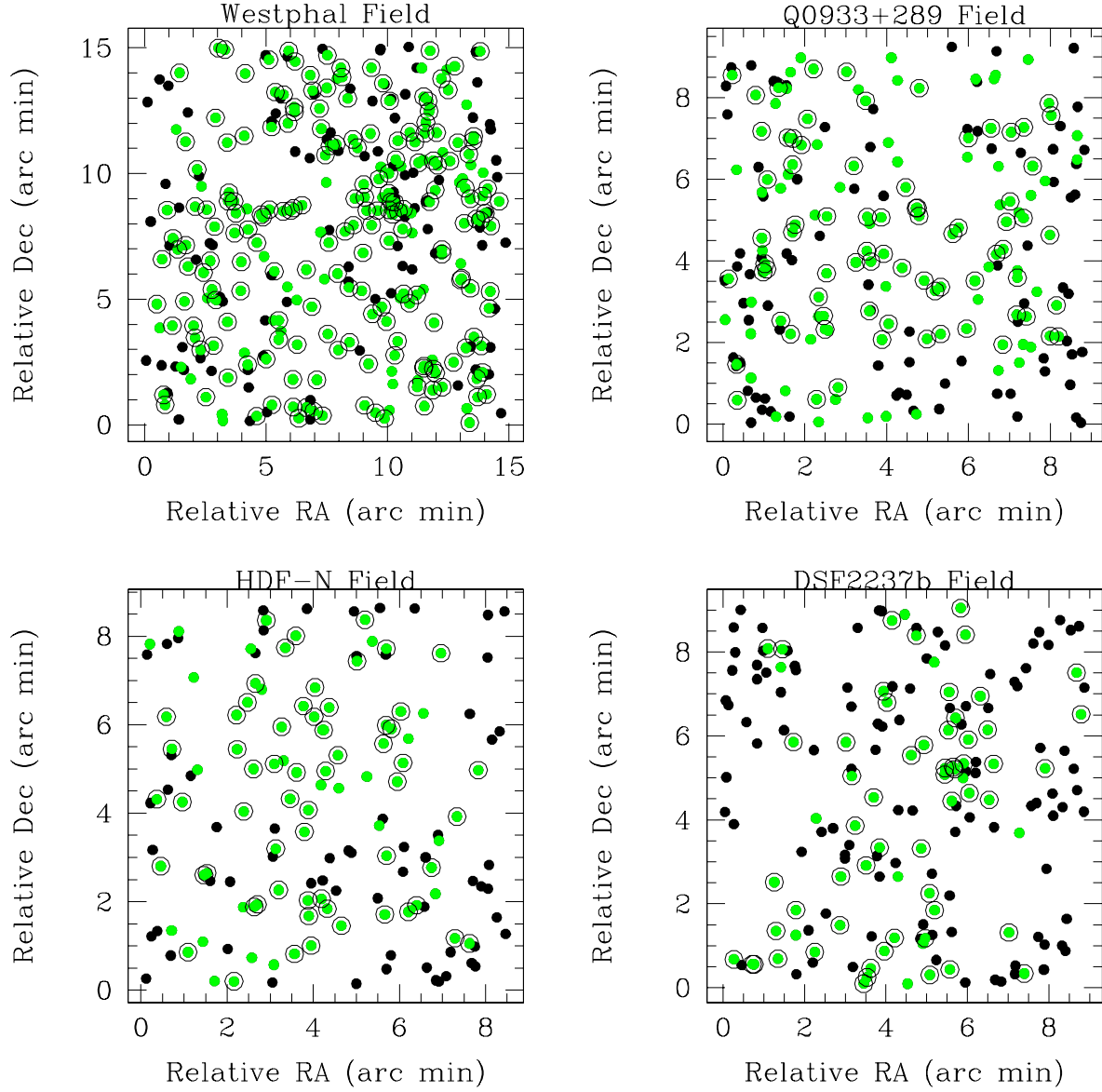
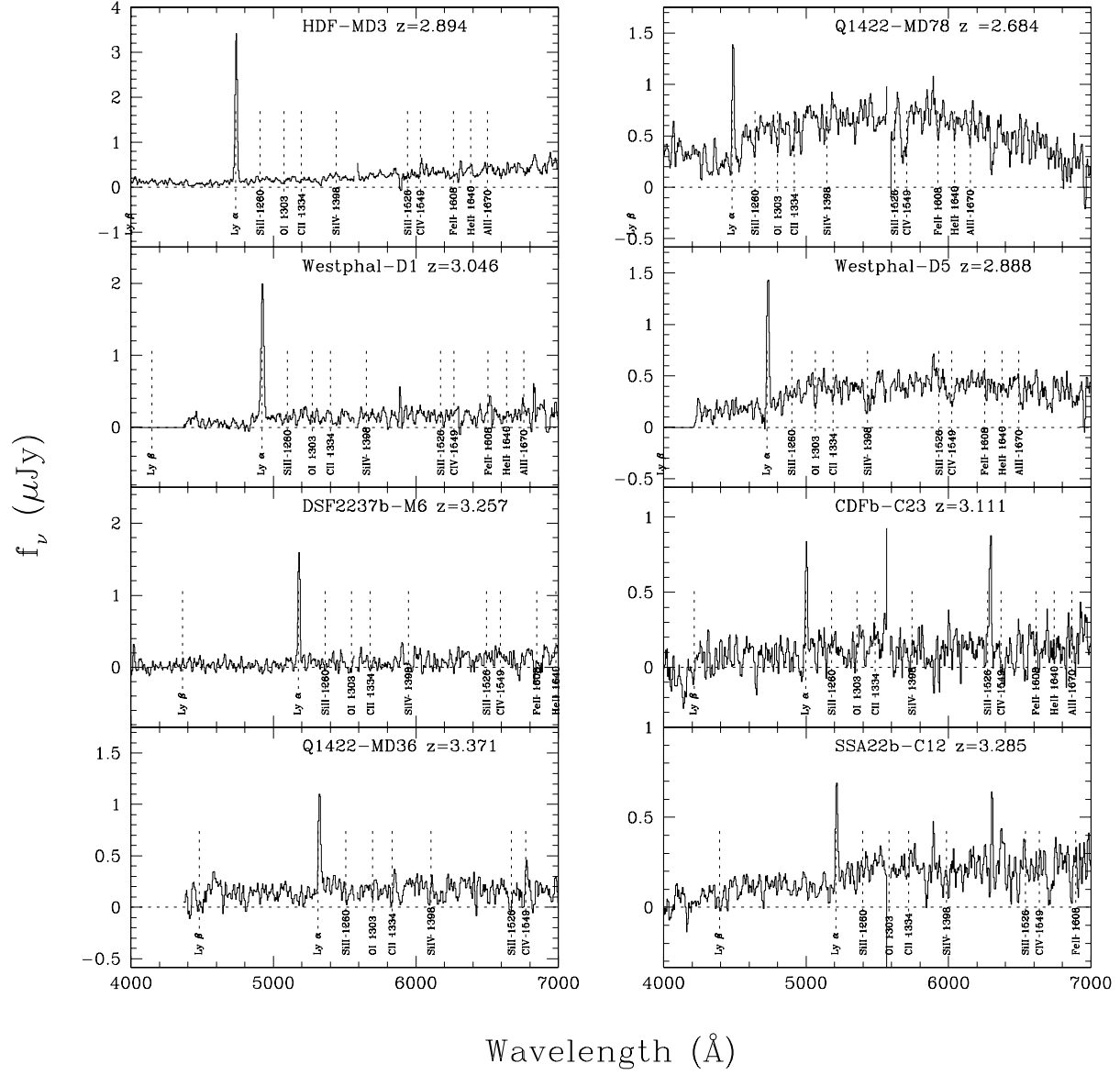


Fig. 7.— Field maps of 4 of the survey fields; all dots are photometrically selected LBG candidates. Green dots are objects that have been observed spectroscopically, and green dots with circles have spectroscopic redshifts $z > 2$.



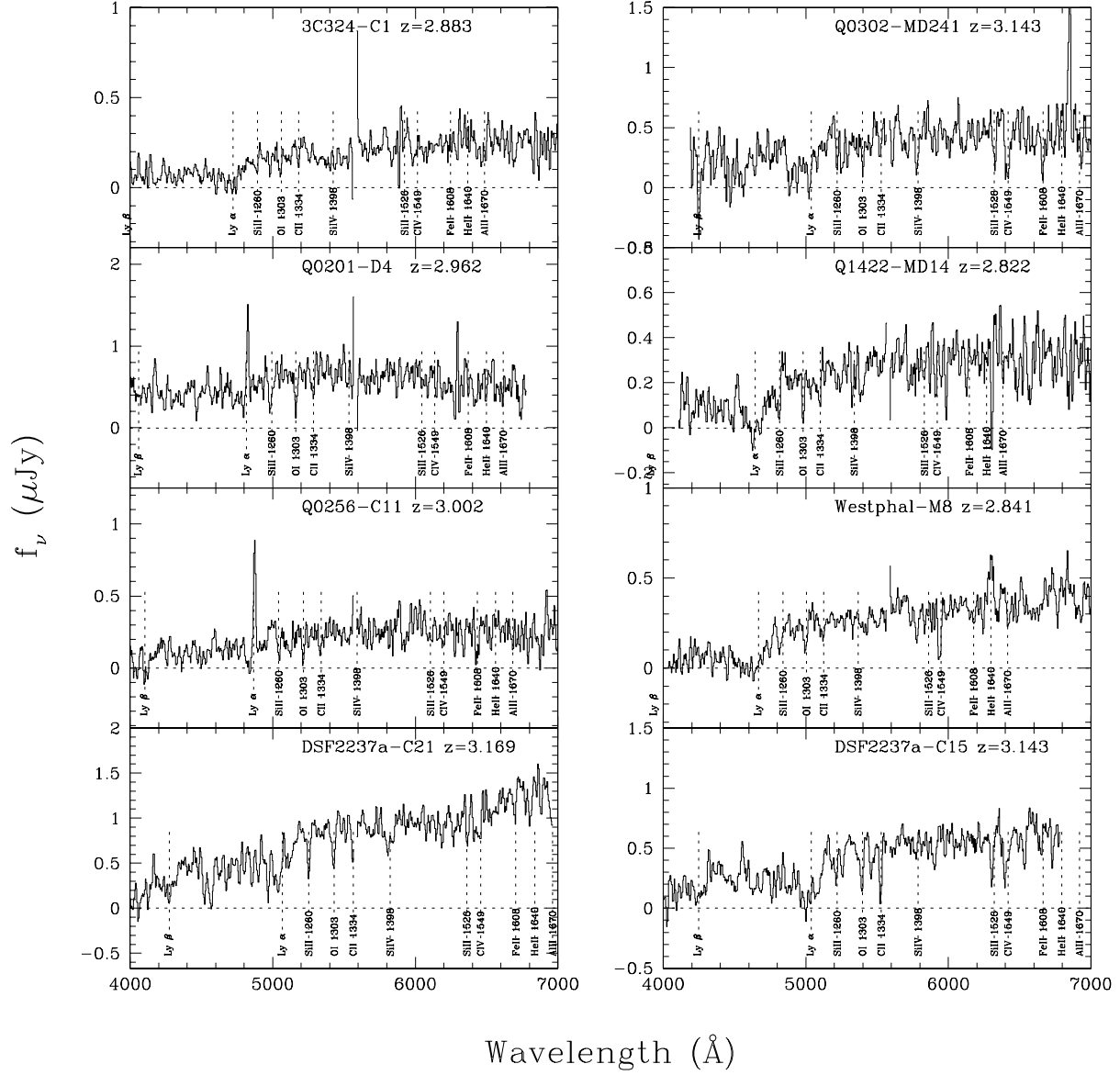


Fig. 8.— Representative spectra of LBGs in the sample. These are intended to be typical of spectra in the full sample, and to cover the range of spectral properties encountered. They were chosen randomly from within lists of spectra grouped by the equivalent width of the Lyman α feature. The spectra have been rebinned to 4.8 \AA per pixel (approximately 2 original pixels and half of a resolution element) and smoothed with a 3-pixel tapered box-car for display purposes.

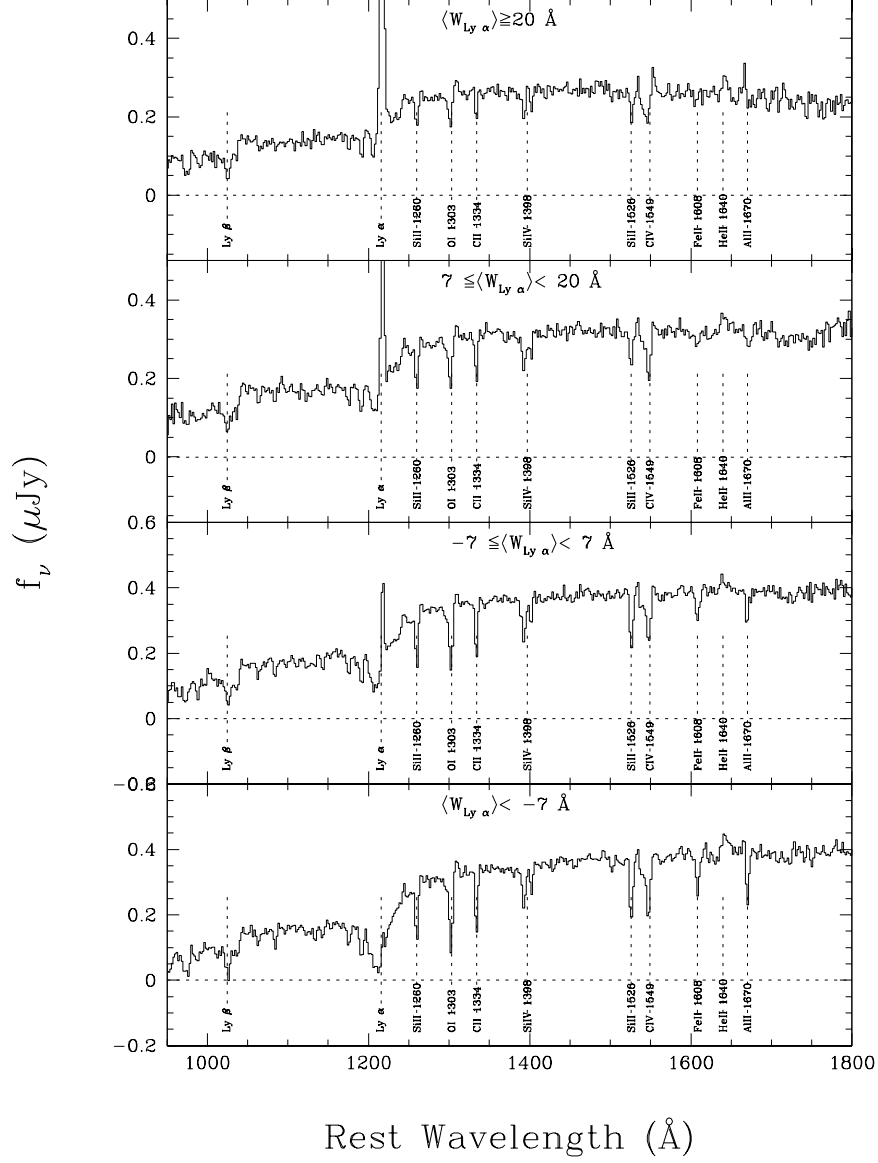


Fig. 9.— Composite spectra of LBGs formed from ~ 200 spectra in each of 4 bins in Lyman α emission strength. The plots have been scaled to emphasize the continuum features in the spectra. Significant trends discernible in the composite spectra are discussed in Shapley et al. 2003.

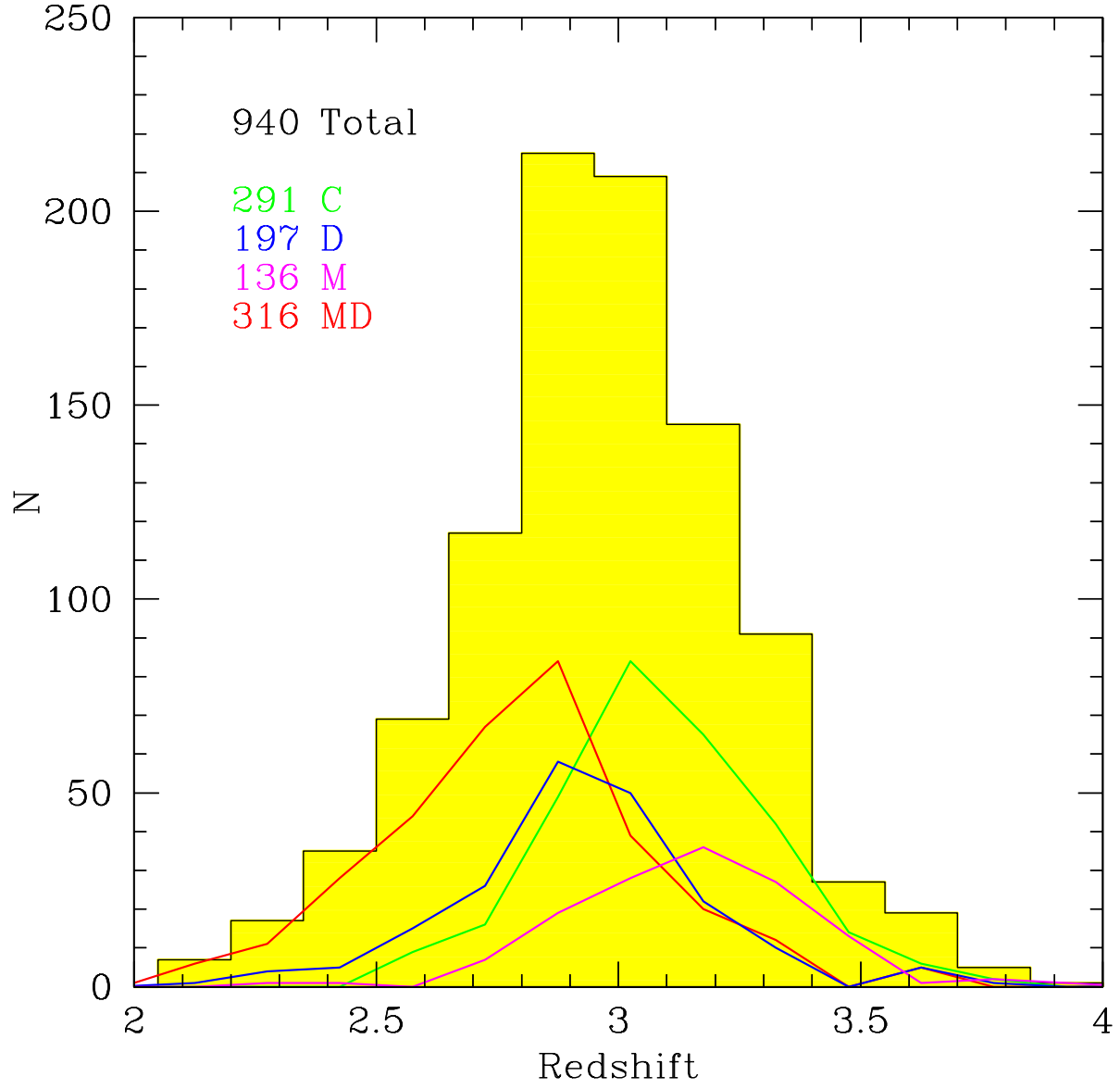


Fig. 10.— Redshift histogram for the objects satisfying the the $z \sim 3$ LBG color selection criteria (Table 4). Also shown are the histograms for each type of candidate (C/D/M/MD). The statistics are summarized in Table 6.

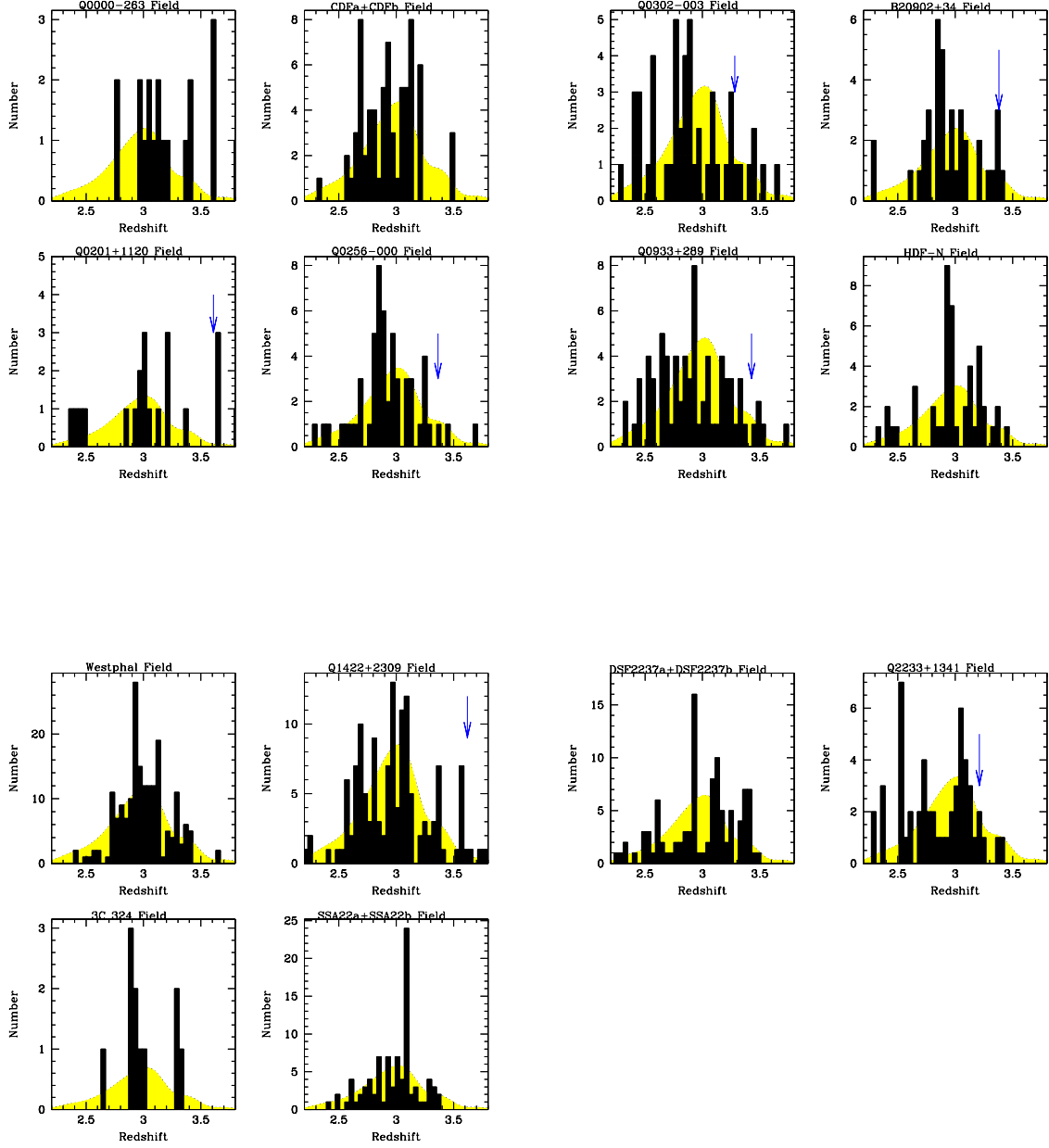


Fig. 11.— Redshift histograms for individual fields, including only those objects satisfying the LBG color criteria. The light colored histogram is the redshift distribution for the full sample, normalized to the number of objects with redshifts in each field. In cases where the survey fields were centered on the positions of known QSOs or high redshift radio galaxies, an arrow marks the redshift for that object. In the case of SSA22, DSF2237, and CDF, adjacent survey fields have been combined.

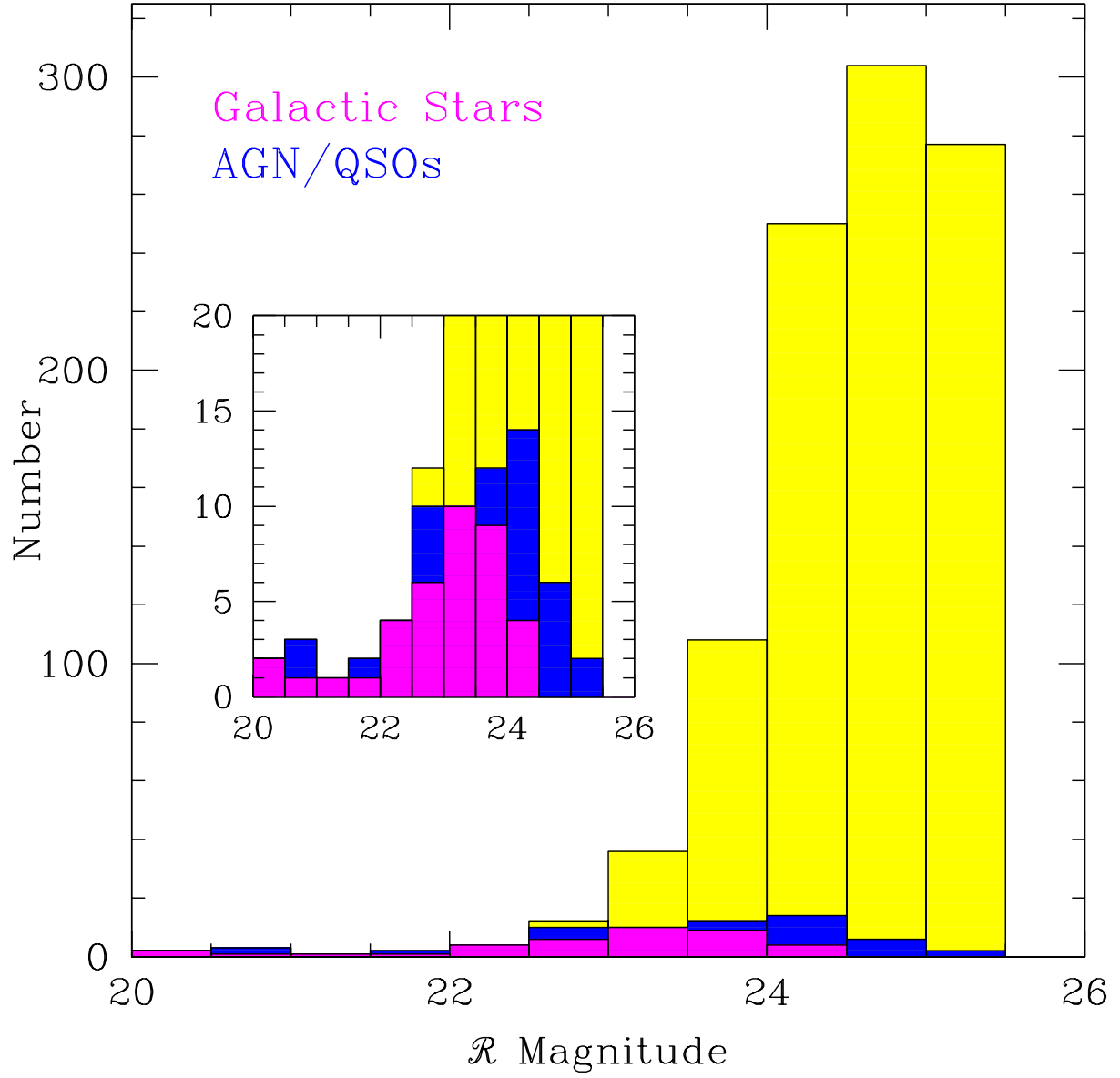


Fig. 12.— Histogram of the apparent magnitude distribution of the contamination of the LBG sample by stars (magenta) and AGN/QSOs (blue; added to the stellar histogram so that the height of stars + AGN/QSOs is the total contamination of the sample) relative to the entire spectroscopically identified sample (yellow). Note that the bright end of the magnitude distribution is dominated by stellar and AGN contamination, but by $\mathcal{R} = 24$, there is essentially no stellar contamination and the AGN contamination is only a few percent.